ICES REPORT 11-15

May 2011

A multiscale method coupling network and continuum models in porous media I single phase flow

by

J. Chu, B. Engquist, M. Prodanovic, R. Tsai

The Institute for Computational Engineering and Sciences
The University of Texas at Austin
Austin, Texas 78712

Reference: J. Chu, B. Engquist, M. Prodanovic, R. Tsai, "A multiscale method coupling network and continuum models in porous media I single phase flow", ICES REPORT 11-15, The Institute for Computational Engineering and Sciences, The University of Texas at Austin, May 2011.

A multiscale method coupling network and continuum models in porous media I – single phase flow

J. Chu, B. Engquist, M. Prodanović, R. Tsai

Abstract

We propose a numerical multiscale method for coupling a conservation law for mass at the continuum scale with a discrete network model that describes the microscale flow in a porous media. In this work we focus on coupling pressure equations. Evaluating pressure from a detailed network model over a large physical domain is typically computationally very expensive. We assume that over the same physical domain there exists an effective mass conservation equation at the continuum scale which could have been solved can be solved efficiently *if the equation was explicitly given.* Our coupling method uses local simulations on sampled domains at network scale to evaluate the continuum equation and thus solve for the pressure in the domain. We allow nonlinearity in the network model as well as the mass conservation equation. Convergence of the coupling method is analyzed. In the case where classical homogenization applies, we prove convergence of the proposed multiscale solutions to the homogenized equations. Numerical simulations are presented.

1 Introduction

In this paper, we develop a new multiscale model for computing pressure of flow in porous media. The algorithm has the form of the heterogeneous multiscale method (HMM)[23], and couples pore scale with continuum scale over the same physical domain.

Modeling multi-phase fluid flow in the subsurface is a notoriously difficult challenge. One must account for processes occurring on a broad range of scales; typically different modeling approaches are needed at different length scales so that the underlying physics can be properly described. At the pore scale, direct simulation in a detailed medium size geometry assuming Stokes flow is extremely costly. Model reduction at the pore scale is normally done by mapping the pore space onto a representative network of idealized pores and throats and then modeling fluid displacements as discrete events on the pore-throat network. For overview of network models see [43, 14, 48]. At larger scales, one usually constructs Darcy's law continuum models in which individual grid blocks contain sufficiently many pores such that the system within each grid block evolves smoothly with time. The specific micro structure of the pore space frequently

plays a critical role in determining macroscopic flow properties, and often cannot be ignored. Continuum models capable of accounting for two scales - the so-called dual porosity models [3, 4, 39]- have been constructed, and some efforts have also been made to build hybrid models [9, 53]. In [9], Balhoff et al. focused on a scenario in which a pore network domain is connected to a continuum Darcy model for solving single phase fluid flow. In their setting, the network domain and continuum domain are physically disjoint except for a shared interface where information from either domains are exchanged. In [10], they improved on the computational complexity and simplifying assumptions of the previous paper, by adapting mortar methods [5] to include pore scale models.

In this paper, we propose a multiscale numerical method that couples network models and continuum equations for subsurface flows over larger length scales. Coupling of network model and continuous equations has been used in [46], done by Rossa, D'Angelo and Quarteroni, to model traffic flows in complex network. In their work, the PDEs at the continuum scale are explicitly derived from network models defined over regular lattice. The coefficients in the PDE can be computed from locally averaging the microscopic solutions. In contrast, in our work, we only assume mass conservation at the continuum level, but otherwise no explicit assumptions on the exact form of the equations. We do not assume regular connectivity in the network models either.

To make our introduction more concrete, consider the following simple setting with a single incompressible fluid at steady state. The fluid velocity $\mathbf{v}$ depends on pressure P, pressure gradient ∇P and the background geological data. The dependence of geological data is described by the location variable $\mathbf{x}$. Mass conservation implies

$$\nabla \cdot \mathbf{v}(\mathbf{x}, P, \nabla P) = S(\mathbf{x}), \tag{1}$$

where S is a source or sink term. In classical models, the flux velocity is assumed to satisfy Darcy's law. That is, $\mathbf{v}$ is proportional to the negative pressure gradient $-\nabla P$ and $\mathbf{v} = -\kappa(\mathbf{x})\nabla P$. The positive definite tensor function $\kappa(\mathbf{x})$ is called permeability. In this case, equation (1) is an elliptic partial differential equation (PDE), and many multiscale methods discuss how to upscale the permeability tensor from finer to coarser scales.

There is a large literature on numerical upscaling from one continuum Darcy equation to another without smaller scales in the permeability. One type of methods is finite element approach with special basis functions that are computed by solving local homogeneous PDEs subject to special boundary conditions. The primitive form of this method can be traced back to the early work of Babuška, Caloz and Osborn [8, 7] who introduced special basis functions for 1D elliptic problems with rough coefficients. Hou and Wu [37] generalized this idea to developed the multiscale finite element method (MsFEM) for multi-dimensional problems with multiscale coefficients. The further convergence analysis of the method can be found in [37, 38]. Later on Efendiev, Hou et al. have applied multiscale finite element/volume method to two-phase flow in porous media problems [27, 28, 21, 19, 1]. For more discussions on the theory and applications of MsFEM, refer to a recent book by Efendiev and Hou [29].

The heterogeneous multiscale method (HMM) [23], introduced by E and Engquist, is a general framework for designing multiscale method by exploiting special structure of problems. HMM starts with an overall macroscopic model that may miss some constitutive relations for macrovariables on the macrogrid. The missing quantities and data in the macroscopic model are obtained by solving an accurate microscale model locally with minimal cost. The HMM framework has been applied to several different multiscale applications: material science [41], complex fluids [44], homogenization [26, 2], stochastic ODEs [50, 25], highly oscillatory dynamical systems [22, 31, 6], wave propagation [30]. More details can be found in a review paper by E et al [24]. Recently, Young and Mitran [52] proposed an HMM-type algorithm to model and compute the deformation of fibrous materials. In the context of homogenization for elliptic problems, in contrast to MsFEM, HMM only uses partial information in microscale model to extract missing data to construct approximated homogenized coefficient to increase efficiency. Also in the particular case of homogenization, the algorithm proposed in this paper can be interpreted as a finite volume HMM for homogenization of elliptic problems. In the Appendix, we present a proof of convergence of the solutions computed by the proposed algorithm to the homogenized solutions.

Traditionally, the absolute permeability field in reservoir simulations is assumed to be given and unchanged, but in reality it might change in time. Such situations may arise due to damage in porous media such as opening or closing of fractures. Dynamic updates of the permeability field is then needed via local microscopic simulation.

In this paper, the macroscopic model is given by (1) and pore scale network models are used as micro-models. In the macro-model, the explicit form of $\mathbf{v} = -K(x)\nabla P$ is not assumed since we want to obtain equivalent information of $\mathbf{v}$ directly from suitably chosen network models of reduced size. More precisely, we shall evaluate the flux $F = \int_\Sigma \mathbf{v} \cdot \mathbf{n}\, ds$ through suitable surfaces Σ for different profiles of pressure P. On the other hand, the macro-quantities (macroscopic pressure, velocity, or flux) can determine if the microscopic configurations will change, for example, by widening throats or growing fractures. The updated microscopic configurations are then used to compute new pressure flux. The two scale computation is iterated until the system converges.

2 The HMM scheme for a model problem

In this section, we present and analyze the proposed multiscale coupling algorithm for problems involving networks that describe media over two or three dimensional domains but the effective continuum equations lies in one dimension. The purpose is to have a simpler setting where the results can be compared with full network simulations and analytic homogenization. The results are generalized to higher dimensions in later sections.

2.1 Network Models at the Microscopic Scale

Network flow modeling, pioneered by Fatt [32, 33, 34], provides a method to link the microscale description of the medium (topology and geometry) with macroscopic fluid properties. A network model aims at good representation of pore and throat interconnectivity in a porous medium. While pores and throats are depicted via simple geometrical shapes, the models retain a subset of the realistic microscale properties (such as pore/throat size or coordination number distribution). Network models essentially bring capillarity and viscosity together, and in contrast with averaging/homogenization approaches, stress capillary forces and their control of flow through the connected network of pores (openings, pore bodies, sites) and throats (narrow channels, necks, bonds). Reviews on network flow models by Celia et al. [18] and Blunt et al. [14, 15] have more details on the models and their historical development.

Theoretical predictions of macroscopic two-phase flow in a porous medium can be achieved by averaging of Navier-Stokes equations on the pore level assuming certain appropriate boundary condition. However, obtaining a closed system of averaged equations requires the introduction of constitutive relationships between the different parameters, such as capillary pressure-saturation and relative permeability-saturation. These relationships can be obtained (or approximated) from simulations on suitably set up networks. Network models are used, for example, to study relation among saturation, capillary pressure and interfacial area [43], predict properties such as permeability [17, 42], imbibition and drainage curves [36], phase distributions, relative permeability [42, 49, 51] and wettability [20].

In network models, pores are simply represented as nodes and throats as links (in simplest form they are cylindrical tubes). The nodes and tubes are usually depicted by vertices and edges respectively. Thus a network model has a topology of a graph. However, as each pore has a physical location, we shall refer a network that models a medium in a d dimensional domain as a d dimensional network. See Figure 1 for an illustration of a two dimensional network.

For convenience, we number all nodes in the domain and collect them in the set I. Furthermore, we shall denote by $I^{(0)}$ the index set containing all the indices of the nodes lying in the interior of the network domain. Let I_i denote the set consisting of all node indices j that connect to the node i by a throat. Further, p_i denotes the microscopic pressure inside pore i and c_{ij} denotes the conductance of the throat which connects pore i and the pore j for each $j \in I_i$. The pressure flux from pore i to pore j is simply $c_{ij}(p_i - p_j)$.

The conductance for a Newtonian fluid in a cylindrical throat is computed exactly using Hagen-Poiseulle solutions and is given by

$$c_{ij} = \frac{\pi r^4}{8\, l \mu},$$

where r is the radius and l the length of the throat, and μ is the viscosity of the fluid. In general, the conductance c_{ij} may be a nonlinear function,

$$c_{ij} := c(p_i, p_j), \tag{2}$$

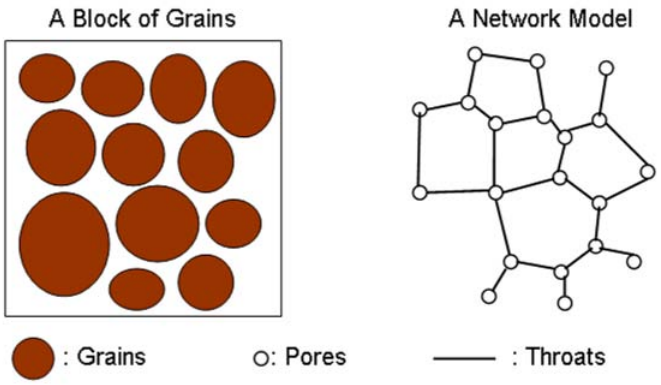

Figure 1: An example of the correspondence of a block of grains and a network model. In the network model, the grains are neglected, the pores are represented by balls (nodes) and the throats are represented by cylindrical tubes (segments).

depending on the nearby pressure p_i and p_j.

The law of mass conservation leads to

$$\sum_{j \in I_i} c_{ij}(p_i - p_j) = s_i, \tag{3}$$

where s_i is the sink or source in the pore i. In most cases, the fluid is assumed incompressible and there are no source or sink term in pores, except at injection or production pores. Therefore, we assume $h_i = 0$ for all $i \in I^{(0)}$ and the system becomes

$$\sum_{j \in I_i} c_{ij}(p_i - p_j) = 0. \tag{4}$$

System (4) should be coupled with suitable boundary conditions on the boundary nodes. The boundary conditions are typically Dirichlet, periodic or Neumann conditions. In this paper, we maintain the following assumption on the length of the throats in the network:

Assumption 2.1. The length of the throats in the network are bounded by a small positive parameter which we denote by ϵ.

In this section, we assume a three dimensional network, and we impose Dirichlet boundary conditions on two opposite faces (the left and the right faces) of the cubic volume and periodic boundary condition (or no flow condition) on the remaining parts of the boundary. Periodic boundary conditions can be used in regular lattice networks, as well as in irregular networks from periodic model sphere packings. Boundary conditions can have a major influence on results, especially if predicting absolute values. While in some cases periodic boundary conditions (on all boundaries) gave better estimates of residual saturations [11] compared to Dirichlet's, the full investigation on the boundary conditions is beyond the scope of this preliminary paper.

Let I_R and I_L denote respectively the index set consisting all indices i such that node i is on the right and the left side face of the domain. We assign $p_i = P_R$ for all $i \in I_R$ and $p_i = P_L$ for all $i \in I_L$. Due to conservation of mass and steady state conditions, the total flux f through the left face of the cuboid domain is the same as the flux through the right

$$f = \sum_{i \in I_L} \sum_{j \in I_i} c_{ij}(p_i - p_j) = -\sum_{i \in I_R} \sum_{j \in I_i} c_{ij}(p_i - p_j). \tag{5}$$

In fact, f is equal to sum of the flux in throats on any cross the section perpendicular the left-right direction. Since f is completed determined by c_{ij} and P_R, P_L, we denote the flux f by $f(P_L, P_R)$ if there is no ambiguity. The function f is the total flow rate in left-right direction caused by the pressures P_L, P_R applied on the left face and the right face.

When there is no source or sink inside the network, we can expect the minimum and maximum pressure of the network is attained on the boundary. We put the proof in the Appendix. See Lemma A.1. Therefore if $P_R = P_L$, then $p_i = P_R$ for all i, and $f(P_L, P_L) = 0$. This fact induces that there exits a nonnegative function q such that

$$f(P_L, P_R) = -(P_R - P_L)q(P_L, P_R). \tag{6}$$

when f is differentiable with respect to P_R and P_L. In particular, if conductances c_{ij} of the network are independent of the boundary conditions as well as the pressures in the pores, the resulting linear system (4) is always solvable. In this case, the function $q(P_L, P_R)$ can be expressed as a constant k/δ, where δ is the distance between left face and right face. Moreover, we can define the permeability κ of the network by

$$\kappa = \frac{k}{A},$$

where A is the area of the left-side face, and the velocity $\mathbf{v}$ satisfies the Darcy's law:

$$\mathbf{v} = \frac{f}{A} = \frac{-k(P_R - P_L)}{A\delta} = -\kappa \nabla P.$$

See Lemma A.2 for more detail. However, when the network model is nonlinear, the maximal-minimal principle still holds, but q may not be a constant function and $f(P_L, P_R)$ depends on P_L and P_R nonlinearly.

2.2 Macroscopic Continuum Model

Consider a network model over the domain $[x_L, x_R] \times [y_1, y_2] \times [z_1, z_2]$. We impose Dirichlet on the boundaries at x_L and x_R, and periodic boundary condition (or no flow Neumann) on the other 4 faces. Let $B_\delta(x)$ be the subdomain $[x - \delta/2, x + \delta/2] \times [y_1, y_2] \times [z_1, z_2]$ and $\Sigma(x; \delta)$ be the boundary surface of $B_\delta(x)$. By integrating (1) over $B_\delta(x)$ and using the boundary conditions, we have

$$\int_{B_\delta} S \, dv = \int_{B_\delta} \nabla \cdot \mathbf{v} \, dv = \oint_{\Sigma} \mathbf{v} \cdot \mathbf{n} \, ds = F_{\Sigma_R} - F_{\Sigma_L}, \tag{7}$$

where F_{Σ_R} and F_{Σ_L} are the fluxes through boundaries at $x + \delta/2$ and $x - \delta/2$ respectively. Dividing δ on the both sides of (7) and taking the limit as δ to 0 lead to

$$\frac{d}{dx}F = \lim_{\delta \to 0} \frac{1}{\delta} \int_{B_\delta(x)} S dv \equiv Q(x), \qquad x \in (x_L, x_R). \tag{8}$$

Hence we obtain a one dimensional equation in macroscopic scale, with its corresponding two or three dimensional network model in microscale. The macroscopic domain becomes simply $[x_L, x_R]$ and the unknowns are the macroscopic pressure P and flux F. The macroscopic pressure P can be viewed as an average pressure of small scale pressure p on the cross section $\Sigma(x; 0)$. We assume the flux F is a function of pressure P, pressure gradient P_x and location x. To close the equation (8), the boundary value of pressure $P(x_L) = P_L$ and $P(x_R) = P_R$ are given.

We apply a finite volume discretization for (8). Let N be the number of partitions of $[x_L, x_R]$ and $\Delta x = (x_R - x_L)/N$, $x_l = x_L + l\Delta x$ for $l = 0, 1, ..., N$, . Let P_l be the approximation of $P(x_l)$ and $F_{l-\frac{1}{2}}$ be the approximation of the flux F at $x_{l-\frac{1}{2}} = (x_l + x_{l-1})/2 = x_L + (l - \frac{1}{2})\Delta x$. We assume that the discrete flux $F_{l-\frac{1}{2}}$ is uniquely determined by adjacent pressure P_l and P_{l-1} only. The finite volume discretization of (8) is to find $P_0, P_1, P_2, ..., P_{N-1}, P_N$ such that $P_0 = P_L$, $P_N = P_R$ and

$$F_{l+\frac{1}{2}} - F_{l-\frac{1}{2}} = \int_{x_{l-\frac{1}{2}}}^{x_{l+\frac{1}{2}}} Q dx \equiv Q_i \Delta x \quad \text{for } l = 1, 2, ..., N-1, \tag{9}$$

2.3 Coupling of the macroscopic model and the network model

The macroscopic flux $F_{l-\frac{1}{2}}$ is determined by the network model as follows. For each grid node x_l, we choose a subdomain $B_\delta(x_{l-\frac{1}{2}})$. We shall call the corresponding portion of our network over this subdomain the local network centered at $x_{l-\frac{1}{2}}$. Each of such local network is set up as in Section 2.1 with certain Dirichlet conditions to be discussed below.

- The macroscopic flux $F_{l-\frac{1}{2}}$ is defined as the flux, denoted by $\hat{f}_{l-\frac{1}{2}}$, through the corresponding local network:

  $$F_{l-\frac{1}{2}}(P_{l-1}, P_l) = \hat{f}_{l-\frac{1}{2}}.$$

  This flux through the local network domain with some appropriate boundary conditions.

- The Dirichlet boundary conditions for the subdomain $B_\delta(x_{l-\frac{1}{2}})$ at $x_{l-\frac{1}{2}} \pm \delta/2$ are defined as the values of the macroscopic at the corresponding locations. At the discretization level, they are approximated by linear interpolation of P_l and P_{l-1} on $[x_{l-1}, x_l]$ to define an approximation of the pressure P at $x_{l-\frac{1}{2}} \pm \delta/2$. Thus,

the flux through the local network is a function depending on two macroscopic pressure values and the center of the subdomain

$$\hat{f}_{l-\frac{1}{2}} = f(x_{l-\frac{1}{2}}, P_{l-1}, P_l),$$

where f is the function defined by (5) in Section 2.1. More precisely, the Dirichlet boundary conditions at $x_{l-\frac{1}{2}} \pm \frac{\delta}{2}$ are $P_{l-\frac{1}{2},L}$ and $P_{l-\frac{1}{2},R}$ defined by $P_{l-\frac{1}{2}} = (P_{l-1} + P_l)/2$, and

$$P_{l-\frac{1}{2},L} = P_{l-\frac{1}{2}} - D^+P_{l-1}(\delta/2), \quad P_{l-\frac{1}{2},R} = P_{l-\frac{1}{2}} + D^+P_{l-1}(\delta/2),$$

where $D^+P_{l-1} = (P_l - P_{l-1})/\Delta x$ is the standard divided centered differencing on P_{l-1}.

- The source term $\int_{x_{l-\frac{1}{2}}}^{x_{l+\frac{1}{2}}} Q\,dx = \int_B S dv$ is obtained by summing all source term s_i in each pores inside subdomain B. In particular, $Q_i\Delta x = \int_{x_{l-\frac{1}{2}}}^{x_{l+\frac{1}{2}}} Q dx = 0$ if we assume $s_i = 0$ in the network model.

Figure 2 shows a schematic representation of coupling macroscale and microscale models. Since we only use partial information from the whole network model to estimate the flux locally, and the information of small pressure p in 3D network model is compressed into microscopic pressure P in one dimension, the computational cost is tremendously reduced. Under this setting, *the flux F can be obtained for any given pressures P_{l-1} and P_l, but the explicit expression is unknown, when the underlying network model is nonlinear.* The formal algebraic equations (9) for the macroscopic pressure P_l may be nontrivial to solve as the relation between $F_{l-\frac{1}{2}}$, P_{l-1} and P_l are not available explicitly. In particular, the Newton's method is not applicable and thus an alternate root finding scheme is required. We propose a quasi-Newton-like scheme in next section.

2.4 Macro-Micro Iterative Scheme

From the previous section, we see that the flux through a point in the macroscopic domain can be evaluated from the flux through the corresponding local network. It remains to recover the pressure values in the macroscopic domain. The difficulty to be overcome here is that no convenient analytical relation between the macroscopic flux F and the pressure P is available (or rather assumed). In the following discussion, we first assume that there is no source term in the system.

At the discrete level, we want to solve the following equations for P_l:

$$F(x_{l+\frac{1}{2}}, P_{l+\frac{1}{2}}, D^+P_l) = \hat{f}_{l+\frac{1}{2}}(P_l, P_{l+1}). \tag{10}$$

$$D^-F(x_{l+\frac{1}{2}}, P_{l+\frac{1}{2}}, D^+P_l) = Q_l\Delta x,\ l = 1, 2, \cdots, N-1, \tag{11}$$

with the boundary condition $P_0 = P_L, P_N = P_R$. See Figure 2 for a diagram. We propose to solve the above coupled equations by simple iterations roughly as follows:

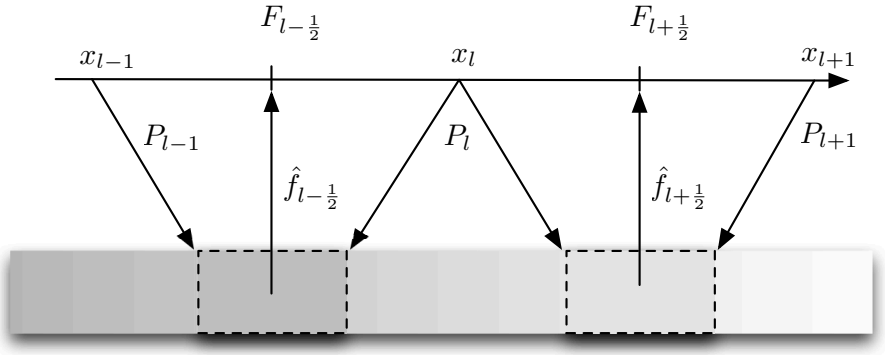

Figure 2: Continuous (macro) scale is discretized using points $x_l, l = 0, .., N$. Macro flux $F_{l-\frac{1}{2}}$ is updated using micro scale simulation (network model) on a representative region within the segment $[x_{l-1}, x_l]$ (local network domain). At the same time, the boundary conditions (in this sketch, pressure boundary conditions) required for the micro-scale model come from the macro-scale information (pressure) at end points $[x_{l-1}, x_l]$.

The left hand side of Equation (11) will be approximated using $P_l^{(n+1)}$ as well as $P_l^{(n)}$. We start out from a fundamental assumption that

$$F(x, P, P_x) = f(x, P, P_x) = 0, \quad \text{whenever } P_x = 0.$$

Suppose further that F is smooth, then mean value theorem suggests that

$$F(x, P, P_x) = F_{P_x}(x, P, \xi)P_x, \tag{12}$$

where F_{P_x} refers to the partial derivative of F with respect to third variable and ξ is an intermediate value, which depends on P and x, between 0 and P_x. Therefore, we use

$$F_{P_x}(x, P, \xi) \approx \hat{f}_{l+\frac{1}{2}}(P_l, P_{l+1})/D^+P_l =: -K(P_l, P_{l+1}). \tag{13}$$

Hence, the iterative scheme becomes:

$$-D^-\left(K(P_l^{(n)}, P_{l+1}^{(n)})D^+P_l^{(n+1)}\right) = Q_l\Delta x. \tag{14}$$

We next describe details of the algorithm. We shall see, from (19) and (20), that our proposed scheme can be interpreted as a type of quasi-Newton method at the macroscopic level for solving the nonlinear equation that is evaluated by a set of local network simulations.

Algorithm 2.2. Start with an initial guess $\mathbf{P}^{(0)} = [P_0^{(0)}, P_1^{(0)}, ..., P_N^{(0)}]^T$ with $P_0^{(0)} = P_L$, $P_N^{(0)} = P_R$ and $P_l^{(0)} \neq P_{l-1}^{(0)}$ for all $l = 1, 2, ..., N$. A conventional choice is the linear interpolation of the boundary conditions. That is, $P_l^{(0)} = l\Delta x(\frac{P_R - P_L}{x_R - x_L}) + P_L$.

For $n = 0, 1, ...$

1. Evaluate $F^{(n)}_{l-\frac{1}{2}} = \hat{f}_{l-\frac{1}{2}}(P^{(n)}_{l-1}, P^{(n)}_{l})$ for $l = 1, 2, ..., N$.

2. Compute the effective parameter $K^{(n)}_{l-\frac{1}{2}}$ and construct the matrices $\mathbf{K}^{(n)}$ and $\mathbf{h}^{(n)}$ as defined below:

$$K^{(n)}_{l-\frac{1}{2}} = F^{(n)}_{l-\frac{1}{2}} \cdot \frac{\delta}{(P^{(n)}_{l-\frac{1}{2},L} - P^{(n)}_{l-\frac{1}{2},R})} = -\frac{F^{(n)}_{l-\frac{1}{2}}}{D^+P^{(n)}_{l-1}}, \tag{15}$$

$$\mathbf{K}^{(n)} = \begin{pmatrix} K^{(n)}_{\frac{1}{2}} + K^{(n)}_{\frac{3}{2}} & -K^{(n)}_{\frac{3}{2}} & 0 & \cdots & 0 \\ -K^{(n)}_{\frac{3}{2}} & K^{(n)}_{\frac{3}{2}} + K^{(n)}_{\frac{5}{2}} & -K^{(n)}_{\frac{5}{2}} & \ddots & \vdots \\ 0 & -K^{(n)}_{\frac{5}{2}} & \ddots & \ddots & 0 \\ \vdots & \ddots & \ddots & \ddots & -K^{(n)}_{N-\frac{3}{2}} \\ 0 & \cdots & 0 & -K^{(n)}_{N-\frac{3}{2}} & K^{(n)}_{N-\frac{3}{2}} + K^{(n)}_{N-\frac{1}{2}} \end{pmatrix}, \tag{16}$$

$$\mathbf{h}^{(n)} = [Q_1 + K^{(n)}_{1-\frac{1}{2}} P_L/\Delta x^2, Q_2, ..., Q_{N-2}, Q_{N-1} + K^{(n)}_{N-\frac{1}{2}} P_R/\Delta x^2]^T. \tag{17}$$

3. Update $\mathbf{P}^{(n+1)}$ by solving the linear equation

$$\mathbf{K}^{(n)}\mathbf{P}^{(n+1)} = \Delta x^2 \mathbf{h}^{(n)}.$$

Alternatively, define

$$\mathbf{G}(\mathbf{P}) = \left[D^+F_{1-\frac{1}{2}} - Q_1, D^+F_{2-\frac{1}{2}} - Q_2, ..., D^+F_{N-1-\frac{1}{2}} - Q_{N-1}\right]^T \tag{18}$$

The solution of (9) is the root of $\mathbf{G}$. By using the relation $F^{(n)}_{l-\frac{1}{2}} = -K^{(n)}_{l-\frac{1}{2}} D^+P^{(n)}_{l-1}$, we have $\mathbf{G}(\mathbf{P}^{(n)}) = \frac{1}{\Delta x^2}\mathbf{K}^{(n)}\mathbf{P}^{(n)} - \mathbf{h}^{(n)}$, where $\mathbf{K}^{(n)}$ and $\mathbf{h}^{(n)}$ are defined in the same way as before. We have

$$\mathbf{P}^{(n+1)} = (\frac{1}{\Delta x^2}\mathbf{K}^{(n)})^{-1}\mathbf{h}^{(n)} = \mathbf{P}^{(n)} - (\frac{1}{\Delta x^2}\mathbf{K}^{(n)})^{-1}\mathbf{G}(\mathbf{P}^{(n)}). \tag{19}$$

Stop when a chosen numerical convergence criterion is met.

Remark 2.3. The proposed iterative scheme has several good properties. The matrices $\mathbf{K}^{(n)}$ are symmetric positive definite and tridiagonal. Therefore the linear equation $\mathbf{K}^{(n)}\mathbf{P}^{(n+1)} = \Delta x^2 \mathbf{h}^{(n)}$ can be solved in $\mathcal{O}(N)$ operations (for example by Cholesky decomposition), and the solution $P^{(n+1)}$ satisfies max-min property. That is, $P^{(n+1)}_l$ is between the boundary value P_L and P_R. This guarantees the proposed macro-micro iterative scheme will never show numerical blowup.

Remark 2.4. When there is no source term inside the network model, it is not hard to see $P_l^{(n)} - P_{l-1}^{(n)} \neq 0$ for all l and n unless boundary the conditions P_L and P_R are the same. However, when there is a nonzero source (or when considering 2D and 3D macroscopic models discussed in Section 2.4.1), $P_l^{(n)} - P_{l-1}^{(n)}$ can be zero for some l and n. In this case the effective coefficient $K_{l-\frac{1}{2}}^{(n)}$ is not well defined and we estimate $K_{l-\frac{1}{2}}^{(n)}$ by

$$K_{l-\frac{1}{2}}^{(n)} = -\hat{f}_{l-\frac{1}{2}}(P_{l-1}^{(n)}, P_{l-1}^{(n)} + \Delta P) \cdot \frac{\Delta x}{\Delta P},$$

where ΔP is a small positive number(we choose 10^{-12} in our numerical experiments).

First we show if the scheme is convergent, it converges to a solution of (9).

Lemma 2.5. *If* $\mathbf{P}^{(n)}$ *converges to* $\mathbf{P}^* = [P_1^*, P_2^*, ..., P_N^*]^T$ *as* n *tends to infinity, then* $P_1^*, P_2^*, ..., P_N^*$ *solve equation* (9).

Proof. By substituting $K_{l-\frac{1}{2}}^{(n)}$ in (15) into the linear equation $\mathbf{K}^{(n)}\mathbf{P}^{(n+1)} = \Delta x^2 \mathbf{h}^{(n)}$, we have

$$\left(\frac{F_{l+\frac{1}{2}}^{(n)}}{D^+P_l^{(n)}}\right) D^+P_l^{(n+1)} - \left(\frac{F_{l-\frac{1}{2}}^{(n)}}{D^+P_{l-1}^{(n)}}\right) D^+P_{l-1}^{(n+1)} = Q_l \Delta x$$

By taking the limit, we have $F_{l+\frac{1}{2}}^* - F_{l-\frac{1}{2}}^* = Q_l \Delta x$ for $l = 1, 2, ..., N$ and hence we have $\mathbf{G}(\mathbf{P}^*) = 0$. □

In classical models, the conductances c_{ij} in the network model depend on geological structure only and are assumed constant in time. In this case, the proposed method is identical to the classical upscaling methods and no iteration is needed for solving $\mathbf{P}$.

Lemma 2.6. *Suppose the conductance* c_{ij} *in the network model for computing the flux* $f_{i-\frac{1}{2}}$ *is independent of both macroscopic pressure* $\mathbf{P}$ *and microscopic pressure* $\mathbf{p}$*, then the macro-micro iteration scheme converges in one step. Moreover, the proposed iterative scheme coincides with the Newton's method.*

Proof. By Lemma A.2, the effective parameter $K_{l-1/2}^n$ is independent of $\mathbf{P}^{(n)}$ and therefore independent of n. It follows $\mathbf{P}^{(1)}$ and $\mathbf{P}^{(n)}$ satisfy the same linear system and hence $\mathbf{P}^{(1)} = \mathbf{P}^{(n)}$ for all n. Since $K_{l-\frac{1}{2}}^{(n)}$ is independent of $\mathbf{P}^{(n)}$, it is easy to check $\frac{1}{\Delta x^2}\mathbf{K}^{(n)} = \frac{\partial \mathbf{G}}{\partial \mathbf{P}}(\mathbf{P}^{(n)})$, the Jacobian of $\mathbf{G}$ at $\mathbf{P}^{(n)}$, and the iteration is just Newton's method. □

For general flux functions $F_{l-\frac{1}{2}}$, (19) still holds in our method, but $\frac{1}{\Delta x^2}\mathbf{K}$ is not equal to the Jacobian of $\mathbf{G}$. Recall that

$$F_{l-\frac{1}{2}}(P_l, P_{l-1}) = \hat{f}_{l-\frac{1}{2}}(P_{l-1}, P_l) = -K_{l-\frac{1}{2}}(P_l, P_{l-1}) D^+P_{l-1}$$

for some nonnegative function $K_{l-\frac{1}{2}}(P_l, P_{l-1})$. If $K_{l-\frac{1}{2}}$ is differentiable with respect to P_l and P_{l-1}, a direct computation shows that the Jacobian of G is

$$\mathbf{J} = \frac{\partial \mathbf{G}}{\partial \mathbf{P}} = \frac{1}{\Delta x^2}\mathbf{K} + \frac{1}{\Delta x^2}\mathbf{A}, \tag{20}$$

where $\mathbf{A}$ is tridiagonal with

$$\mathbf{A}_{l,k} = (P_l - P_{l+1})\frac{\partial K_{l+\frac{1}{2}}}{\partial P_k} - (P_{l-1} - P_l)\frac{\partial K_{l-\frac{1}{2}}}{\partial P_k}, \quad \text{for } k = l-1, l, l+1 \tag{21}$$

Therefore our method is a quasi-Newton's method derived by discarding the matrix $\mathbf{A}$ in Jacobian of $\mathbf{G}$.

Theorem 2.7. *Let $\mathbf{P}^*$ be a root of $\mathbf{G}$. Suppose there exists $\eta > 0$ and constants M and $\lambda < 1$ such that $K_{l-\frac{1}{2}}$ are C^2 for $l = 1, 2, ...N$ and $\|\mathbf{K}^{-1}\| \leq M$, $\|\mathbf{K}^{-1}\mathbf{A}\| \leq \lambda$ whenever $\|\mathbf{P} - \mathbf{P}^*\| < \eta$. Then there exists $\eta^* > 0$ such that for initial vector $\mathbf{P}^{(0)}$ satisfies $\|\mathbf{P}^{(0)} - \mathbf{P}^*\| < \eta^*$, the sequence $\mathbf{P}^{(n)}$ generated by the scheme converges to $\mathbf{P}^*$.*

Proof. Since $K_{l-\frac{1}{2}}$ are C^2 for $l = 1, 2, ...N$ for $\|\mathbf{P} - \mathbf{P}^*\| < \eta$, Taylor expansion of $\mathbf{G}$ at $\mathbf{P}$ is

$$0 = \mathbf{G}(\mathbf{P}^*) = \mathbf{G}(\mathbf{P}) + \mathbf{J}(\mathbf{P})(\mathbf{P}^* - \mathbf{P}) + \mathbf{R}(\mathbf{P}),$$

where $\mathbf{J}$ is the Jacobian of $\mathbf{G}$, and the remainder $\mathbf{R}(\mathbf{P})$ satisfies $\|\mathbf{R}(\mathbf{P})\| \leq R_1\|\mathbf{P} - \mathbf{P}^*\|^2$ for some constant R_1. Therefore, for $\|\mathbf{P}^{(n)} - \mathbf{P}^*\| < \eta$

$$\mathbf{G}(\mathbf{P}^{(n)}) = -\mathbf{J}(\mathbf{P}^{(n)})(\mathbf{P}^* - \mathbf{P}^{(n)}) - \mathbf{R}(\mathbf{P}^{(n)})$$

Combining with (20) leads to

$$\mathbf{P}^{(n+1)} = \mathbf{P}^{(n)} - (\frac{1}{\Delta x^2}\mathbf{K}^{(n)})^{-1}\mathbf{G}(\mathbf{P}^{(n)}) = \mathbf{P}^* + \mathbf{K}^{-1}\mathbf{A}(\mathbf{P}^{(n)})(\mathbf{P}^* - \mathbf{P}^{(n)}) + \Delta x^2\mathbf{K}^{-1}\mathbf{R}(\mathbf{P}^{(n)}) \tag{22}$$

Let $R_2 = MR_1\Delta x^2$ and $\eta^* = \min\{\eta, (1-\lambda)/(2R_2)\}$. Assume $\|\mathbf{P^{(n)}} - \mathbf{P}^*\| < \eta^*$, then we have

$$\|\mathbf{P}^{(n+1)} - \mathbf{P}^*\| \leq \lambda\|(\mathbf{P}^{(n)} - \mathbf{P})^*\| + R_2\|\mathbf{P}^{(n)} - \mathbf{P}^*\|^2 \leq (\frac{1+\lambda}{2})\|(\mathbf{P}^{(n)} - \mathbf{P})^*\| < \eta^* \tag{23}$$

Hence by induction, if $\|\mathbf{P}^{(0)} - \mathbf{P}^*\| < \eta^*$

$$\|\mathbf{P}^{(n)} - \mathbf{P}^*\| \leq (\frac{1+\lambda}{2})^n\|(\mathbf{P}^{(0)} - \mathbf{P})^*\| < (\frac{1+\lambda}{2})^n\eta^* \tag{24}$$

which converges to 0. □

Let us summarize a few key points of the proposed algorithms presented above.

1. The effective continuum equation is discretized as in (9), leading to a nonlinear system of equations for the macroscopic pressure P_l.

2. Local network simulations are used to evaluate the nonlinear fluxes F at points designated by the discretization (9).
3. Since no explicit analytic form is available for the macroscopic flux F, in order to solve (9) for P_l, the proposed scheme utilizes an idea from Taylor expansion of the flux function.

Below, we present an example which studies the efficiency of our proposed method as a solver for nonlinear equations. To do this, we ignore the additional difficulties that may be caused by items 2 and 3 listed above by assuming that the analytical form of the macro flux is known and that the values of the flux can be evaluated without any errors. We compare the performance of the proposed scheme to two classical iterative root finding schemes: Newton's method and Broyden's method [16].

Experiment 1. (**Comparison of different nonlinear solvers for computing macro pressure**) Consider the flux function

$$F(P_{l-1}, P_l) = -\left(\frac{P_{l-1}+P_l}{2}\right) D^+ P_{l-1} = \frac{P_{l-1}^2 - P_l^2}{2\Delta x}, \quad \text{for} \quad l = 1, 2, \ldots, N.$$

We look for the solution $\{P_l\}_{l=0}^N$ of the equation

$$F(P_{l-1}, P_l) = F(P_l, P_{l+l}), \quad \text{for} \quad l = 1, 2, \ldots, N,$$

with the boundary conditions $P_0 = 1$ and $P_N = 0$. For the given boundary condition, the exact solution is given by $P_l = \sqrt{1 - l/N}$. Recall that

$$\mathbf{G}(\mathbf{P}) = \left[D^+ F_{1-\frac{1}{2}} - Q_1, D^+ F_{2-\frac{1}{2}} - Q_2, ..., D^+ F_{N-1-\frac{1}{2}} - Q_{N-1}\right]^T,$$

where $F_{l-\frac{1}{2}} := F(P_{l-1}, P_l), l = 1, 2, \cdots, N-1$, and the solution $\mathbf{P} = (P_0, P_2, \cdots, P_N)^T$ is the root of $\mathbf{G}(\mathbf{P})$. In this example, $Q_l = 0$ for all l. Thus, in this setup, Newton's method, the proposed method and Broyden's method are all of the same form:

$$\mathbf{P}^{(n+1)} = \mathbf{P}^{(n)} - \left(\mathbf{M}^{(n)}\right)^{-1} \mathbf{G}(\mathbf{P}^{(n)}),$$

with different choices for the matrix $\mathbf{M}^{(n)}$.

- Newton's method: $\mathbf{M}^{(n)} = \mathbf{J}(\mathbf{P}^{(n)})$, the Jacobian of $\mathbf{G}$ at $\mathbf{P}^{(n)}$. The Jacobian $\mathbf{J}$ in this example is a tridiagonal matrix with $\mathbf{J}_{l,l} = P_l/\Delta x^2$, $\mathbf{J}_{l,l+1} = -P_{l+1}/(2\Delta x^2)$ and $\mathbf{J}_{l+1,l} = -P_l/(2\Delta x^2)$
- The proposed method: $\mathbf{M}^{(n)} = \mathbf{K}^{(n)}/\Delta x^2$ as described in (19). The $\mathbf{K}$ in this example is tridiagonal with $\mathbf{K}_{l,l} = (P_{l-1} + 2P_l + P_{l+1})/2$ and $\mathbf{K}_{l,l+1} = \mathbf{K}_{l+1,l} = -(P_{l+1} + P_l)/2$.
- The Broyden's method: $\mathbf{M}^{(n)}$ is a rank-one updated matrix constructed from $\mathbf{M}^{(n-1)}$ that satisfies

$$\mathbf{M}^{(n)}\left(\mathbf{P}^{(n)} - \mathbf{P}^{(n-1)}\right) = \mathbf{G}(\mathbf{P}^{(n)}) - \mathbf{G}(\mathbf{P}^{(n-1)})$$

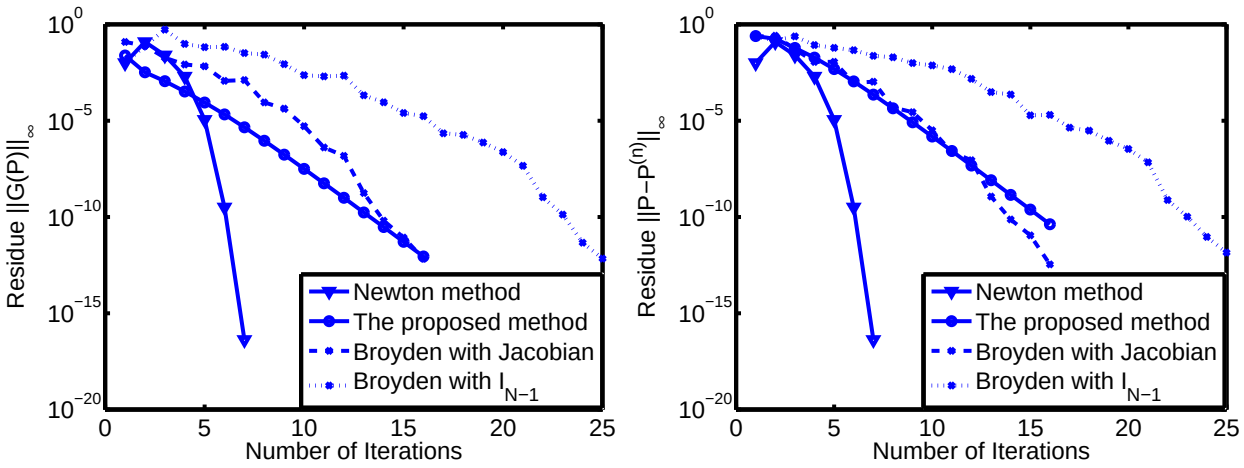

Figure 3: Comparison of 3 different iteration methods for the testing problem with $N = 10$

and

$$\mathbf{M}^{(n)}\mathbf{Q} = \mathbf{M}^{(n-1)}\mathbf{Q}, \quad \forall \mathbf{Q} \perp \left(\mathbf{P}^{(n)} - \mathbf{P}^{(n-1)}\right)$$

The initial matrix $\mathbf{M}^{(0)}$ is typically chosen to be the Jacobian of $\mathbf{G}$ at $\mathbf{P}^{(n)}$ or the identity matrix $\mathbf{I}$.

We first remark that in general $\mathbf{J}$ is not necessary symmetric but $\mathbf{K}$ used in our scheme is.

For all tested methods, the initial guess in this experiment is chosen to be $P_l^{(0)} = 1 - l/N$. The stopping criteria for three methods is the norm of the residual $\|\mathbf{G}(\mathbf{P}^{(n)})\|_\infty < 10^{-12}$. In the Broyden's scheme we set the initial matrix $\mathbf{M}^{(0)}$ to be either the Jacobian $\mathbf{J}(\mathbf{P}^{(0)})$ evaluated at the initial guess or the identity matrix $\mathbf{I}_{N-1}$.

The number of partitions N is chosen to be 10 and 50. When $N = 10$, in Figure 3, it shows all three methods converge to the correct solution. Newton's method requires the fewest iterations to converge. Broyden's method with Jacobian as initial matrix and the proposed method need almost the same number of iterations. Broyden's method with I_{N-1} as initial matrix converges slightly more slowly. We can see the initial guess of matrix $\mathbf{M}^{(0)}$ is important for Broyden's method. When $N = 50$, in Figure 4, it shows only Newton's method and the proposed method converge to the correct solution. Broyden's method diverges for either choice of $\mathbf{M}^{(0)}$. The numbers of iterations are similar to the number of iterations used in the case $N = 10$ for Newton's and the proposed methods. It suggests that both methods do not suffer from higher dimensionality of solution in this particular example and that the performance of our scheme is comparable to Newton's method.

2.4.1 Presence of Source Terms

In previous discussions, we assume there is no source term in the network model. This is not the case when there are injection and production domains inside the network

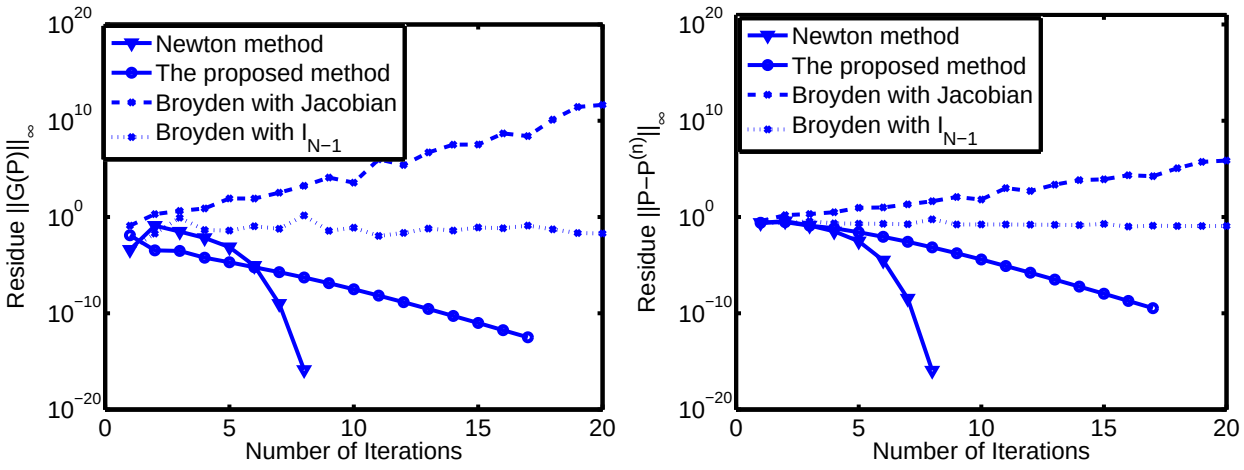

Figure 4: Comparison of 3 different iteration methods for the testing problem with $N = 50$

model. Recall that S and s_i are the source or sink terms in the continuous equation (1) and network model (3) respectively. When $s_i \neq 0$ for some i the microscopic flux depends on boundary conditions, source term s_i inside the network model and the location of the cross section Σ_x. Denote those s_i inside the local network domain $B_\delta(x_{l-\frac{1}{2}})$ by $\mathbf{s}_{l-\frac{1}{2}}$. The local flux of the local network domain $B_\delta(x_{l-\frac{1}{2}})$ is defined by

$$\hat{f}_{l-\frac{1}{2}}(P_{l-1}, P_l, \mathbf{s}_{l-\frac{1}{2}}) = \sum_{i \in I_{C_L}} \sum_{j \in I_{C_R}} c_{ij}(p_i - p_j), \tag{25}$$

where p_i is the solution of the conservation law (3) with source or sink terms $\mathbf{s}_{l-\frac{1}{2}}$ and the index set I_{C_L} and I_{C_R} consist indices $i \in I_{C_L}$ and $j \in I_{C_R}$ such that pore i is on the left hand side of the central cross section $\Sigma_{x_{l-\frac{1}{2}}}$ and pore j is on the right hand side. The macroscopic flux now is defined by $F_{l-\frac{1}{2}}(P_{l-1}, P_l) = \hat{f}_{l-\frac{1}{2}}(P_{l-1}, P_l, \mathbf{s}_{l-\frac{1}{2}})$.

In the one dimensional models, the discretized system (9) becomes finding $\{P_l\}_{l=0}^N$ such that $P_0 = P_L$, $P_N = P_R$ and

$$\hat{f}_{l+\frac{1}{2}}(P_{l+1}, P_l, \mathbf{s}_{l+\frac{1}{2}}) - \hat{f}_{l-\frac{1}{2}}(P_{l-1}, P_l, \mathbf{s}_{l-\frac{1}{2}}) = Q_l \Delta x \tag{26}$$

Here we require the average source term Q_l satisfies the compatible condition:

$$Q_l \Delta x = \int_{B_{\Delta x}(x_l)} S dv = \sum_{i \in I_l} s_i,$$

where the index set I_l is the collection of index i such that pore i is inside the domain $B_{\Delta x}(x_l) = [x_l - \Delta x/2, x_l + \Delta x/2] \times [y_1, y_2] \times [z_1, z_2]$. The condition holds when we have information about the full network model or we have statistic data of the network model. Notice that in this case, $\hat{f}_{l-\frac{1}{2}}(P_{l-1}, P_l, \mathbf{s}_{l-\frac{1}{2}})$ may not vanish when $P_l = P_{l-1}$.

Therefore, there may not exit a function q such that $\hat{f}_{l-\frac{1}{2}}(P_{l-1}, P_l, \mathbf{s}_{l-\frac{1}{2}}) = (P_l - P_{l-1})q(P_{l-1}, P_l)$ as before and we can not apply our macro-micro iteration directly.

When the network model is linear, we can modify the equation to apply our algorithm. By linearity of the solution of the network model, we have

$$\hat{f}_{l-\frac{1}{2}}(P_{l-1}, P_l, \mathbf{s}_{l-\frac{1}{2}}) = f_{l-\frac{1}{2}}(P_{l-1}, P_l) + \hat{f}_{l-\frac{1}{2}}(0, 0, \mathbf{s}_{l-\frac{1}{2}}), \tag{27}$$

where $f(P_{l-1}, P_l)$ is the flux obtained from network model with zero source as defined in Section 2.1. The system of equation (26) is rewritten as

$$f_{l+\frac{1}{2}}(P_{l+1}, P_l) - f_{l-\frac{1}{2}}(P_{l-1}, P_l) = Q_l \Delta x - \hat{f}_{l+\frac{1}{2}}(0, 0, \mathbf{s}_{l+\frac{1}{2}}) + \hat{f}_{l-\frac{1}{2}}(0, 0, \mathbf{s}_{l-\frac{1}{2}}).$$

The right hand side is independent of P_l and can be computed easily. After obtaining the right hand side, we apply our macro-micro scheme to get P_l and the solution is convergent in one step since the system is linear.

The decomposition (27) is no longer valid in the case of nonlinear networks with source terms. Suppose that for a given macro pressure, P_{l-1} and P_l, we solve the corresponding local nonlinear network model and obtain the pressure $\tilde{p}_i$ at node i. Then we evaluate the flux $\hat{f}$ according to (25). With the computed pressure $\{\tilde{p}_i\}$, we define an equivalent linear network model by the conductance $\tilde{c}_{ij} := c(\tilde{p}_i, \tilde{p}_j)$. Denote by $\hat{f}^L_{l-\frac{1}{2}}(P_{l-1}, P_l, \mathbf{s}_{l-\frac{1}{2}}; \{\tilde{c}_{i,j}\})$ the flux in the linear network model with conductance $\tilde{c}_{ij}$, boundary conditions P_{l-1}, P_l and source term $\mathbf{s}_{l-\frac{1}{2}}$. Obviously, with $\tilde{c}_{ij}$ defined by the solution of the local nonlinear network, we have the following identity

$$\begin{aligned} \hat{f}_{l-\frac{1}{2}}(P_{l-1}, P_l, \mathbf{s}_{l-\frac{1}{2}}) &= \hat{f}^L_{l-\frac{1}{2}}(P_{l-1}, P_l, \mathbf{s}_{l-\frac{1}{2}}; \{\tilde{c}_{i,j}\}) && (28) \\ &= f^L_{l-\frac{1}{2}}(P_{l-1}, P_l; \{\tilde{c}_{i,j}\}) + \hat{f}^L_{l-\frac{1}{2}}(0, 0, \mathbf{s}_{l-\frac{1}{2}}; \{\tilde{c}_{i,j}\}), && (29) \end{aligned}$$

where $f^L_{l-\frac{1}{2}}(P_{l-1}, P_l; \{\tilde{c}_{i,j}\}) = \hat{f}^L_{l-\frac{1}{2}}(P_{l-1}, P_l, \mathbf{0}; \{\tilde{c}_{i,j}\})$. Under this setting f^L satisfies the property $f^L_{l-\frac{1}{2}}(P_{l-1}, P_l; \{\tilde{c}_{i,j}\}) = 0$ if $P_{l-1} = P_l$ and we can use it to find solution of (26). by our macro-micro iteration. We summarize the macro-micro iterative scheme for nonlinear network model with nonzero source for 1D Model as following

Algorithm 2.8. Start with an initial guess $\mathbf{P}^{(0)} = [P_0^{(0)}, P_1^{(0)}, ..., P_N^{(0)}]^T$ with $P_0^{(0)} = P_L$, $P_N^{(0)} = P_R$ and $P_l^{(0)} \neq P_{l-1}^{(0)}$ for all $l = 1, 2, ..., N$.

For $n = 0, 1, ...$

1. Solve nonlinear network model to get obtain the pressure $\{p_i^{(n)}\}$ and then evaluate the flux $\hat{f}_{l-\frac{1}{2}}(P_{l-1}^{(n)}, P_l^{(n)}, \mathbf{s}_{l-\frac{1}{2}})$ according to (25).

2. Create a new linear network model with conductance $c_{ij}(p_i^{(n)}, p_j^{(n)})$ to compute $\hat{f}^L_{l-\frac{1}{2}}(0, 0, \mathbf{s}_{l-\frac{1}{2}})$ and define

$$f^{(n)}_{l-\frac{1}{2}} = \hat{f}_{l-\frac{1}{2}}(P_{l-1}^{(n)}, P_l^{(n)}, \mathbf{s}_{l-\frac{1}{2}}) - \hat{f}^L_{l-\frac{1}{2}}(0, 0, \mathbf{s}_{l-\frac{1}{2}}; \{\tilde{c}^{(n)}_{i,j}\})$$

3. Compute the effective parameter

$$K^{(n)}_{l-\frac{1}{2}} = -f^{(n)}_{l-\frac{1}{2}}/D^+P^{(n)}$$

and construct the matrix $\mathbf{K}^{(n)}$ as in (16) and $\mathbf{h}^{(n)}$ defined by

$$\mathbf{h}^{(n)}_l = \begin{cases} Q_1 - D^+\hat{f}^{(n)}_{1-\frac{1}{2}} + K^{(n)}_{\frac{1}{2}}P_L\Delta x^{-2}, & l=1 \\ Q_l - D^+\hat{f}^{(n)}_{l-\frac{1}{2}}, & 1<l<N \\ Q_N - D^+\hat{f}^{(n)}_{N-\frac{1}{2}} + K^{(n)}_{N-\frac{1}{2}}P_R\Delta x^{-2}, & l=N, \end{cases}$$

where $\hat{f}^{(n)}_{l-\frac{1}{2}} = \hat{f}^L_{l-\frac{1}{2}}(0,0,\mathbf{s}_{l-\frac{1}{2}};\{\tilde{c}^{(n)}_{i,j}\})$ obtained in (2).

4. Update $\mathbf{P}^{n+1}$ by solving the linear equation

$$\mathbf{K}^{(n)}\mathbf{P}^{(n+1)} = \Delta x^2\mathbf{h}^{(n)},$$

Stop when a chosen numerical convergence criterion is met.

The proof of convergence of the iterative scheme is similar to Theorem 2.7.

2.5 Numerical Experiments

In the following numerical experiments, we compare the results computed from full network simulations and the proposed multiscale simulations. The testing full network model has 1001×20 nodes arranged in a long rectangle domain. Each node is connected by 6 nearby nodes and the length of throats are 1 unit in horizontal and vertical direction, and are $\sqrt{2}$ unit in diagonal direction. The radii of the throats are randomly generated from the uniform distribution $[(1-\lambda)r_0,(1+\lambda)r_0]$ and the conductance c is determined by

$$c = \frac{\pi r^4}{8\,l\mu}.$$

We choose $r_0 = 0.01$, $\lambda = 0.5$, and $\mu = 1$ and the boundary condition is the Dirichlet on x-direction: $p = 100$ on the left hand side and $p = 0$ on the right hand side, and periodic boundary condition in y direction. In the simulations using the proposed mulitscale algorithms, we divide the domain into N blocks, each of the dimension $\delta\times 20$, so that the center of each block corresponds to the node $x_{\frac{l}{2}}$ described in Section 2.3. At the microscopic level, we experimented with a few local networks with different sizes.

In the following experiments, we fix $\delta = 10, 15, 20$ and set $N = 5, 10, 20, 30$ to test the convergence of the proposed algorithm. We compare the flux F_D and the pressure P_D computed from direct full simulation on 1001×20 nodes with the flux F_H and the pressure P_H computed by the proposed multiscale algorithm using either sampling methods. The pressure P_D is the average value of fine scale pressure on each y-direction section. The relative errors of flux e_F and of pressure e_P are defined by

$$e_F = \frac{|F_H - F_D|}{|F_D|} \quad \text{and} \quad e_P = \frac{\|P_H - P_D\|_\infty}{\|P_D\|_\infty},$$

where $\|\cdot\|_\infty$ is the supreme norm of vectors. There are 3 kinds of relations between f_{ij} and the pressure difference $p_i - p_j$ testing in network model simulation: linear flux, quadratic flux in pressure and quadratic flux in velocity.

Experiment 2. (**Linear flux**) This is a standard linear network model in which the flux f_{ij} is given by

$$f_{ij} = -c_{ij}(p_i - p_j).$$

We run 1000 realizations of the radius of each throat to obtain the corresponding conductance c_{ij}. The averaged relative errors e_P and e_F obtained from different N and δ are listed below:

	e_p			e_f		
	$\delta = 10$	$\delta = 15$	$\delta = 20$	$\delta = 10$	$\delta = 15$	$\delta = 20$
$N = 5$	0.0348	0.0284	0.0240	0.0936	0.0626	0.0487
$N = 10$	0.0267	0.0217	0.0185	0.0883	0.0585	0.0440
$N = 20$	0.0195	0.0151	0.0122	0.0864	0.0556	0.0403
$N = 30$	0.0157	0.0115	0.0086	0.0864	0.0554	0.0412

We observe that both errors are well controlled for each parameter. The pressure error decreases as the number of blocks N increases or the sampling size δ increases, but the flux error is mainly controlled by sampling size δ. We will explain how to improve proposed method to get convergence in flux in Section 2.6. The magnitude of the errors indicates that it is suitable to set macroscopic system as an 1D model when conductance is uniformly distributed, even we only use partial information of the whole network model.

Experiment 3. (**Quadratic flux in pressure**) The flux f_{ij} in the network model is given by

$$f_{ij} = -\frac{1}{2}c_{ij}(p_i + p_j)(p_i - p_j),$$

and the conductance is $\frac{1}{2}c_{ij}(p_i + p_j)$ which depends on nearby pressures p_i and p_j. The formula is a simplified version of Poiseuille's equation for compressible fluids [13]:

$$f = \frac{\pi r^4}{16\mu l}\left(\frac{p_i^2 - p_o^2}{p_o}\right) = c\frac{(p_i + p_o)(p_i - p_o)}{2p_o},$$

where p_i is inlet pressure, p_o is outlet pressure. Poiseuille's equation is used for a compressible fluid in a tube the volumetric flow rate and the linear velocity is not constant along the tube.

We use fix point iterations to solve nonlinear network system. We start with the solution $p_i^{(0)}$ of the linear network model with conductance c_{ij}. Then we update the conductance by $\frac{1}{2}c_{ij}(p_i^{(n)} + p_j^{(n)})$ and solve the new pressure $p_i^{(n+1)}$. The process is repeated until $\|p^{(n+1)} - p^{(n)}\|_\infty < 10^{-11}$. The average of errors e_P and e_F among 1000 times realization on each radius of the throat are tabulated below:

	e_p			e_f		
	$\delta = 10$	$\delta = 15$	$\delta = 20$	$\delta = 10$	$\delta = 15$	$\delta = 20$
$N = 5$	0.0137	0.0109	0.0092	0.0373	0.0249	0.0195
$N = 10$	0.0101	0.0083	0.0071	0.0325	0.0217	0.0168
$N = 20$	0.0091	0.0071	0.0057	0.0306	0.0200	0.0150
$N = 30$	0.0072	0.0053	0.0040	0.0306	0.0198	0.0146

Similar to the results from the linear flux case, we observe that the pressure errors decrease as the number of blocks N increases and the flux error is mainly controlled by sampling size δ. For computational cost, the number of iterations for each full network model simulation is around 30 and it takes around 200 seconds on a moderate laptop running at 2.3 GHz. In the simulations using the proposed algorithm and full local sampling, at most 5 iterations is needed for compute each $K_l^{(n)}$ from solving local network problems, and around 10 iterations is needed outer loop to obtained convergent values of $P_l^{(n)}$. The multiscale algorithm with full sampling took 30-60 seconds. In general, larger number of blocks (hence smaller local network domains) results in shorter run time. For partial sampling, we can see the errors are under 10% even we only sample 10% data ($N\delta = 100$) from original domain. The computational time reduces to 10 seconds only to get a full convergent result.

Experiment 4. (**Quadratic flux for high velocity flows**) The flux f_{ij} in the network model is given by

$$\frac{f_{ij}}{c_{ij}} + \beta f_{ij}^2 = -(p_i - p_j).$$

The formula is derived from the Forchheimer equation:

$$-\frac{\mathrm{d}p}{\mathrm{d}x} = \frac{\mu}{\mathbf{K}} \cdot v + \rho\beta v^2,$$

where p is the pressure, v is the flux velocity, $\mathbf{K}$ is the permeability and μ is the viscosity, ρ is the fluid density and β is the non-Darcy coefficient of the porous medium. The Forchheimer equation is the standard equation for describing high-velocity flow in petroleum engineering [35, 47]. In our simulation, by solving the quadratic equation, we used the following formula:

$$f_{ij} = \frac{-1 + \sqrt{1 - 4\beta c_{ij}^2 (p_i - p_j)}}{2\beta c_{ij}} \simeq -\left(c_{ij} + \beta c_{ij}^3 |p_i - p_j|\right)(p_i - p_j)$$

The conductance in this case is $\left(c_{ij} + \beta c_{ij}^2 |p_i - p_j|\right)$ and depends on nearby pressures p_i and p_j. The parameter β is chosen to be 10^{12} on purpose in order to amplify nonlinear effects in our simulations. The average error from 1000 realizations is given below

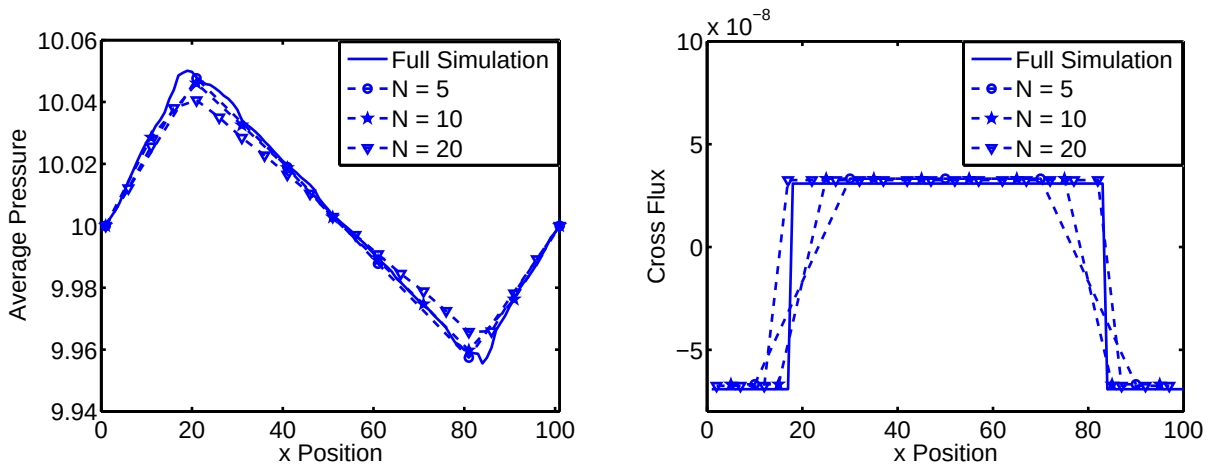

Figure 5: Comparison of pressure and flux obtained from multiscale model and direct simulation.

	e_p			e_f		
	$\delta = 10$	$\delta = 15$	$\delta = 20$	$\delta = 10$	$\delta = 15$	$\delta = 20$
$N = 5$	0.0173	0.0139	0.0114	0.0366	0.0240	0.0193
$N = 10$	0.0127	0.0102	0.0084	0.0322	0.0213	0.0169
$N = 20$	0.0094	0.0071	0.0058	0.0297	0.0193	0.0141
$N = 30$	0.0074	0.0054	0.0041	0.0305	0.0201	0.0150

Experiment 5. (**Presence of source and sink terms in a linear network**) The testing full network model has 101×100 nodes arranged in a rectangle domain and the conductance is chosen randomly as in Experiment 2. The boundary condition is 10 on both left and right sides and periodic in y direction. The source term is zero except $s = 10^{-7}$ at position $(17, 17)$ and $s = -10^{-7}$ at $(83, 83)$. The network is nonlinear with conductance equal to $c_{ij}(p_i + p_j)$. We use the 1D Macro model with blocks $N = 5, 10, 20$ and sampling length is fixed to be 5 in each sampling domain. We compare the average pressure and flux obtained by multiscale model and direct full network model simulation in Figure 5. We can see the proposed method captures the cross flux and average within a reasonable range of error.

2.6 Further Discussion on the Boundary Conditions for Local Network Model

From previous experiments, we notice that flux error of the proposed method is not convergent as number of blocks N increase. To understand this phenomena, we change our setting to fix total size of sampling domain $N\delta$ and vary N. Notice that the total computational cost is approximately proportional to the total size of sampling domain $N\delta$. We choose $N\delta = 40, 100, 200, 400$ and set $N = 3, 5, 7, 10$ to repeat the Experiment 2. The results are shown as dash lines in Figure 6. We observe that both pressure

and flux errors increase as the number of blocks N increases, especially for flux errors. This is due to the artificial boundary condition: the pressure value on the boundary of each block must be the same.

In general, errors from the boundary conditions used in local network simulations dominate the error from the macroscale model which becomes smaller N increases. This explains the why lower number of blocks N resulted in smaller errors, and suggests that Dirichlet boundary condition for the local networks can lead to larger errors in the flux evaluation. In classical homogenization theory, the homogenized coefficient is obtained by solving cell problems and the boundary condition for the cell problem is periodic after subtracting a linear function [12]. Using the similar idea, we can incorporate the macroscopic pressure P_l and P_{l-1} with the flux function $F_{l-\frac{1}{2}}$.

Given macroscopic pressures P_l at x_l, and P_{l-1} at x_{l-1}, we create a microscopic pressure profile p^L on the sampling subdomain $B_\delta(x_{x-\frac{1}{2}})$ by linearly interpolating P_l and P_{l-1} in x-direction. To determine the macroscopic flux $F_{l-\frac{1}{2}}$, we solve the pressure $\tilde{p}$ such that $\tilde{p}$ satisfies the equation (4) on B_δ and $\tilde{p} - p^L$ satisfies periodic condition on the boundary of B_δ. The flux $\tilde{f}_{l-\frac{1}{2}}$ is then defined by

$$\tilde{f}_{l-\frac{1}{2}} = \sum_{i \in I_L} \sum_{j \in I_i} c_{ij}(\tilde{p}_i - \tilde{p}_j),$$

and $F_{l-\frac{1}{2}} = \tilde{f}_{l-\frac{1}{2}}$. Notice that under this construction, $\tilde{p}$ needs not to be the same value on the left or right faces of B_δ and the artificial boundary effect should be reduced. We shall refer this this boundary condition as the "*linearly adjusted periodic boundary condition.*"

By a small modification of Lemma A.2, the solution $\tilde{p}$ is always solvable and unique up to a constant if the network system is linear. We determine the unique solution by choosing $\tilde{p}$ such that the average of $\tilde{p}$ is $P_{l-\frac{1}{2},L} = P_{l-\frac{1}{2}} - D^+P_{l-1}(\delta/2)$ on the left face of B_δ and the average of $\tilde{p}$ on the right face is $P_{l-\frac{1}{2},R} = P_{l-\frac{1}{2}} + D^+P_{l-1}(\delta/2)$, automatically by this choice. We also have that $\tilde{f}(P_{l-1}, P_l) = -kD^+P_{l-1}$ for some constant function k. Hence the macro-micro iteration scheme converges in one iteration.

To compare the performance of two different boundary condition, we testify the same problem in Experiment 2 with linear flux. We perform the comparison for partial sampling method only. The relative errors in pressure e_P and in flux e_F versus different number of sampling blocks N for two different boundary condition are plotted in Figure 6. The result shows that the linearly adjusted periodic boundary condition is slightly worse than Dirichlet boundary condition in fitting the microscopic pressure, but the error in flux is smaller than using Dirichlet boundary condition, and the error is no longer increasing as the number of blocks increase. The error in pressure and flux decrease as the total sampling length $N\delta$ increases. In Figure 7, we present the relative errors as a function of $N\delta$ in log-log plot. The numerical results suggest the error $e_P \sim (N\delta)^{-\alpha}$ and $e_F \sim (N\delta)^{-\beta}$ with α close to 0.59 and β close to 0.58. This implies that for fixed δ(or N) both errors are convergent as N(or δ) increases.

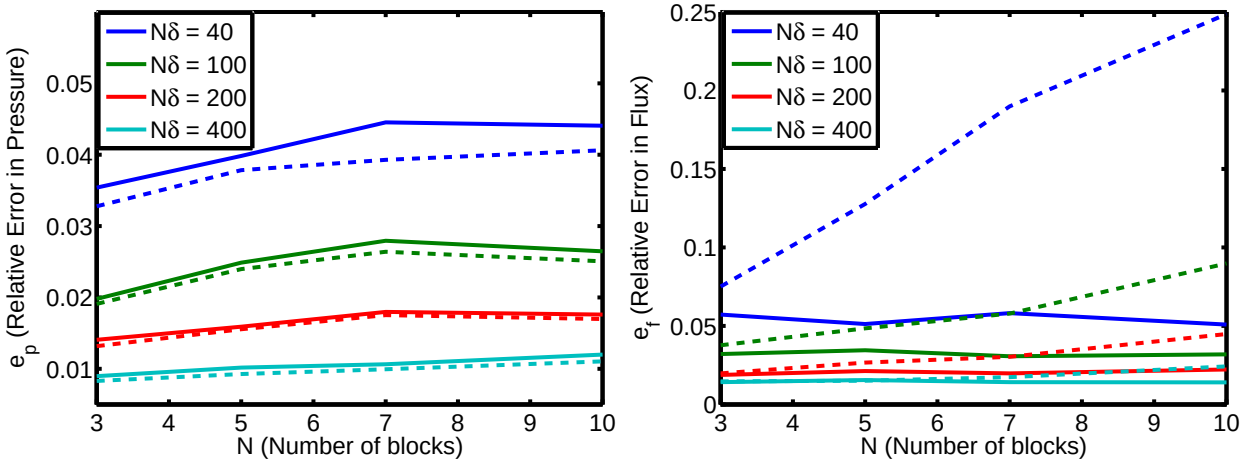

Figure 6: The relative error of pressure e_P (left) and flux e_F (right) versus different number of sampling blocks N for two different boundary conditions. The solid line is for the linearly adjusted periodic boundary condition and the dash line is for Dirichlet boundary condition. Four different color lines stands for different total length of the sampling domain $N\delta$.

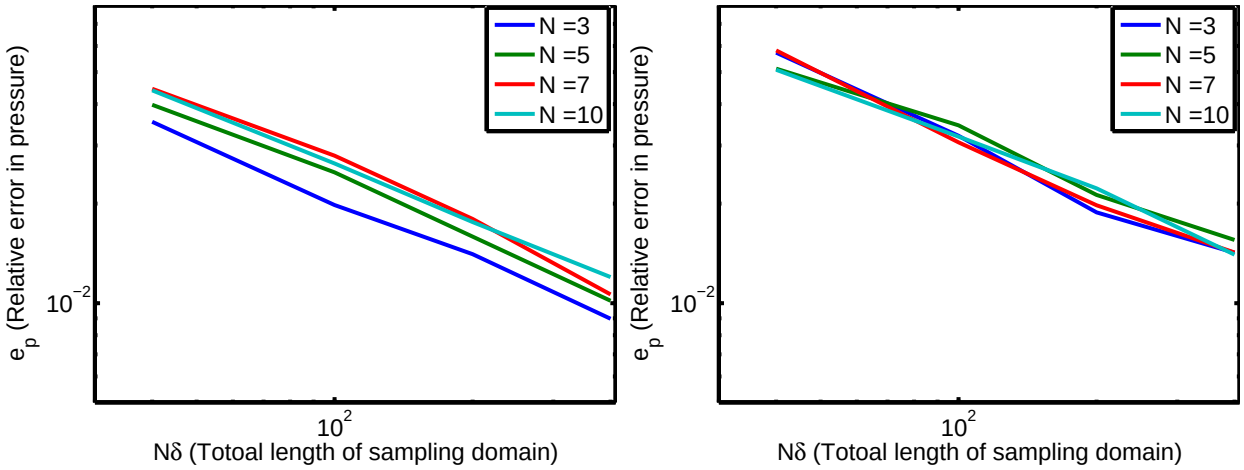

Figure 7: Log-log plot of the relative error of pressure e_P (left) and flux e_F (right) versus different total lengthes of the sampling domain $N\delta$ by using the linearly adjusted periodic boundary condition. Four different color lines stand for different number of blocks N.

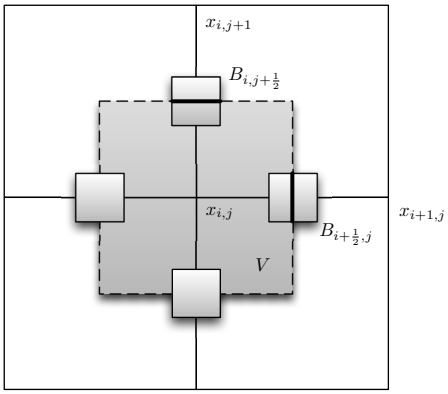

Figure 8: Schematic of 2D macroscale model.

3 Multi-Dimensional Models

In Section 2, a one dimensional macroscopic PDE is coupled with multi-dimensional microscopic network models. Such coupling multiscale models are valid when the variation in the network conductance is predominately in one coordinate direction. In this kind of network models, contours of the microscopic pressure in the network are approximately planar and so it is reasonable to expect a one dimensional macroscopic model. In this section, we describe how our framework can be easily applied to couple multi-dimensional continuum equations with multi-dimensional networks.

We start with the conservation law (1) posed in a rectangular domain with suitable boundary conditions. We use a finite volume discretization to solve the PDE. Divide the domain into $N_1 \times N_2$ coarse blocks. Let $\mathbf{x}_o$ be the center of a block, and V be the corresponding control volume. See Figure (8). Hence, (1) implies that

$$\oint_{\partial V} \mathbf{v} \cdot \mathbf{n} \, ds = \int_V S \, dv = \bar{S}(\mathbf{x}_o) \, \mathrm{Vol}(V), \tag{30}$$

where $\bar{S}$ is the mean of the source term inside V. Let F_N, F_S, F_W, and F_E denote the fluxes through the four edges of V.

$$F_N + F_S + F_W + F_E = \bar{S}(\mathbf{x}_o) \, \mathrm{Vol}(V) \tag{31}$$

We first consider the case in which $S \equiv 0$. Similar to the one dimensional setting, the flux F across each edge is evaluated as $\hat{f}$ coming from local network simulations on a $\delta \times \delta$ size sampling domain B_δ with boundary condition from given pressure P. For instances, F_E and F_N are defined

$$F_E = \mathbf{v}_{i+\frac{1}{2},j} \cdot \mathbf{n}_x \; \Delta y = \hat{f}^{(x)}(P_{i,j}, P_{i+1,j}, P_{i,j+1}, P_{i+1,j+1}, P_{i,j-1}, P_{i+1,j-1})(\Delta y/\delta),$$

$$F_N = \mathbf{v}_{i,j+\frac{1}{2}} \cdot \mathbf{n}_y \; \Delta x = \hat{f}^{(y)}(P_{i,j}, P_{i,j+1}, P_{i+1,j}, P_{i+1,j+1}, P_{i-1,j}, P_{i-1,j+1})(\Delta x/\delta),$$

where $\hat{f}^{(x)}$ and $\hat{f}^{(y)}$ are flux evaluations from the local network simulations described below. In the following discussion, we only present the detail on F_E at $\mathbf{x}_{i+\frac{1}{2},j}$.

As in the one dimensional case, an explicit algebraic formula for the macroscopic flux F as a function of pressure and pressure gradient is not readily available. However, formulas (12) and (14) can be generalized easily since $\mathbf{v} = (v_1, v_2) = \mathbf{0}$ when $\nabla P = 0$. Taylor expansion shows

$$v_1(\mathbf{x}, P, \nabla P) = \partial_{P_x} v_1(\mathbf{x}, P, \xi_1, \xi_2) P_x + \partial_{P_y} v_1(\mathbf{x}, P, \xi_1, \xi_2) P_y, \tag{32}$$

where (ξ_1, ξ_2) are the intermediate values. Then the flux $\hat{f}^{(x)}$ can be approximated by

$$\hat{f}^{(x)}(P_{i,j}, P_{i+1,j}, P_{i,j+1}, P_{i+1,j+1}, P_{i,j-1}, P_{i+1,j-1}) \approx \left((\partial_{P_x} v_1) P_x + \left(\partial_{P_y} v_1\right) P_y \right) \delta,$$

and the pressure gradient ∇P is approximated by forward and central difference of P: $P_x \approx D_+^x P_{i,j}$ and $P_y \approx D_0^y P_{i+\frac{1}{2},j}$, where $P_{i+\frac{1}{2},j} = (P_{i,j} + P_{i+1,j})/2$ and

$$D_0^y P_{i+\frac{1}{2},j} = \frac{P_{i+\frac{1}{2},j+1} - P_{i+\frac{1}{2},j-1}}{2\Delta y} = \frac{(P_{i+1,j+1} + P_{i,j+1}) - (P_{i+1,j-1} - P_{i,j-1})}{4\Delta y}.$$

The flux $\hat{f}^{(x)}$ is evaluated from the local network simulation over $B_\delta(\mathbf{x}_{i+\frac{1}{2},j})$ with the linearly adjusted periodic boundary conditions inspired by a recent work by Engquist, Holst and Runborg [30]. The microscopic pressure p with the condition that $p - p^L$ is periodic on the sampling domain B_δ; here

$$p^L(\mathbf{x}) = U_{i+\frac{1}{2},j} \cdot \mathbf{x} + P_{i+\frac{1}{2},j} \tag{33}$$

with the vector $U_{i+\frac{1}{2},j} = [D_+^x P_{i,j}, D_0^y P_{i+\frac{1}{2},j}]^T$ which is an approximation of ∇P at $\mathbf{x}_{i+\frac{1}{2},j}$, and $\mathbf{x}$ is the position of the pore inside B_δ. The flux $\hat{f}^{(x)}$ is then computed according to (5) by the microscopic pressure p. Another choice of boundary condition for p is the Dirichlet boundary condition: $p = p^L$ on the boundary of B_δ.

The "coefficients" $\partial_{P_x} v_1$ and $\partial_{P_y} v_1$ can be approximated by the additional local network simulations of replacing $U_{i+\frac{1}{2},j}$ in (33) by $[D_+^x P_{i,j}, 0]^T$ and $[0, D_0^y P_{i+\frac{1}{2},j}]^T$ respectively. More precisely, we define $K^{1,1}_{i+\frac{1}{2},j}$ and $K^{1,2}_{i+\frac{1}{2},j}$ as following

$$\begin{aligned} K^{1,1}_{i+\frac{1}{2},j} &= \hat{f}^{(x)}(P_{i,j}, P_{i+1,j}, 0, 0, 0, 0)/(\delta\ D_+^x P_{i,j}), \\ K^{1,2}_{i+\frac{1}{2},j} &= \hat{f}^{(x)}(P_{i+\frac{1}{2},j}, P_{i+\frac{1}{2},j}, P_{i,j+1}, P_{i+1,j+1}, P_{i,j-1}, P_{i+1,j-1})/(\delta\ D_0^y P_{i+\frac{1}{2},j}), \end{aligned} \tag{34}$$

to approximate $\partial_{P_x} v_1$ and $\partial_{P_y} v_1$. Other coefficients $K^{1,1}_{i-\frac{1}{2},j}$, $K^{1,2}_{i-\frac{1}{2},j}$, $K^{2,1}_{i,j\pm\frac{1}{2}}$, $K^{2,2}_{i,j\pm\frac{1}{2}}$ are defined analogously.

Now we are ready to describe our Macro-micro iterations. For a given macroscopic pressure $P^{(n)}_{i,j}$, we compute the coefficients $(K^{1,1}_{i\pm\frac{1}{2},j})^{(n)}$, $(K^{1,2}_{i\pm\frac{1}{2},j})^{(n)}$, $(K^{2,1}_{i,j\pm\frac{1}{2}})^{(n)}$,

$(K^{2,2}_{i,j\pm\frac{1}{2}})^{(n)}$ as in (34). The updated macroscopic pressure $P^{(n+1)}_{i,j}$ is obtained by solving the sparse linear system

$$F^{(n)}_N + F^{(n)}_S + F^{(n)}_W + F^{(n)}_E = 0,$$

where

$$F^{(n)}_E = \left((K^{1,1}_{i+\frac{1}{2},j})^{(n)} D^x_+ P^{(n+1)}_{i,j} + (K^{1,2}_{i+\frac{1}{2},j})^{(n)} D^y_0 P^{(n+1)}_{i+\frac{1}{2},j} \right) \Delta y,$$
$$F^{(n)}_N = \left((K^{2,1}_{i,j+\frac{1}{2}})^{(n)} D^x_0 P^{(n+1)}_{i,j+\frac{1}{2}} + (K^{2,2}_{i,j+\frac{1}{2}})^{(n)} D^y_+ P^{(n+1)}_{i,j} \right) \Delta x.$$

Similar to one dimensional model, the coefficient K's are constant if the network model is linear, and therefore the iteration converges in one step. The Macro-micro iteration is still a quasi-Newton type method and the convergence result can be showed by a modification of proof in Theorem 2.7.

Remark 3.1. When there is non-zero source present in the network model, the local flux $f^{(x)}$ and $f^{(y)}$ involve the network source term $\mathbf{s}$. However, the nonlinearity induced by the source term $\mathbf{s}$ can be removed by the way we introduced in Section 2.4.1.

Experiment 6. (**Two dimensional problem with three disconnected channels with large conductance**) Consider a two dimensional network model with 1001×1000 pores located on a regular lattice. Each grid node in the lattice is connected to six nearby pores as we depicted in Experiment 2. The radius of each throat is a random number chosen from uniform distribution on $[(1-\lambda)r_0, (1+\lambda)r_0]$, except three channels; see Figure 9. The channels are composed by horizontal segment connecting pores (i,j) to $(i+1,j)$, $i \in [1,400]$ and $j \in [245,255]$ for the first channel, $i \in [301,700]$ and $j \in [495,505]$ for the second channel and $i \in [601,1000]$ and $j \in [745,755]$ for the second channel. The radius in the channels is $10r_0$. The pressure corresponding to this network model does not approximate to parallel lines. If we use 1D-model with 5 blocks full sampling to simulate this network model, the relative error of flux is around 2000%. This large error is caused by misinterpreting connection of 3 channels. In 1D-model, each sampling region has a high conductance channel penetrated through, and therefore the regenerative parameter is very high. The induced coarse scale in 1D system has all larger parameters connected together. Three disconnected channels becomes connected and penetrate through the whole region in 1D model, and therefore the computed macroscopic flux is over estimated. To resolve the issue, we need a multi-dimensional macroscopic model.

We divide the domain into $N \times N$ blocks and use $\delta \times \delta$ local network to estimate the macroscopic flux F on each edge of the control volume and apply the proposed 2D model and algorithm. In Table 1, we list the relative pressure error e_P and relative flux error e_F for different numbers of coarse blocks and different sampling domain size. We can see the flux and pressure in 2D-model is significantly improved from the results obtained from 1D model. Notice that the errors decrease as N increase even the our error analysis in Appendix B is not applied in this case. The pressure and flux

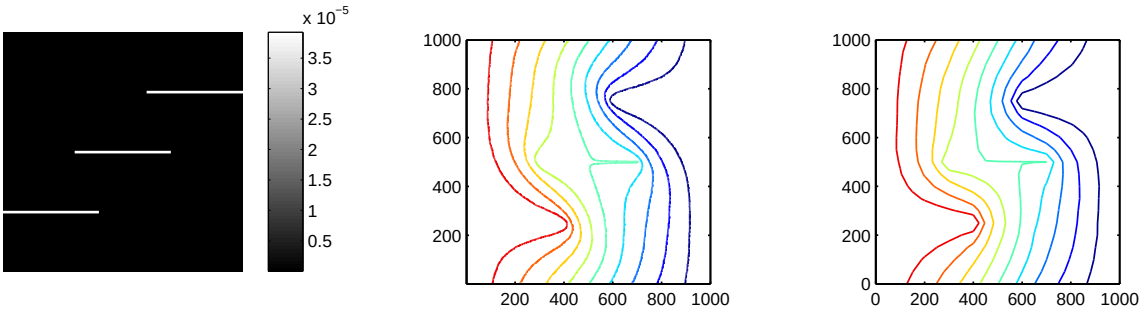

Figure 9: The left subfigure demonstrates the horizontal conductance of the network. The intensity of the image corresponds to the size of the conductance. Three white segments represents the throats with radius equal to $10r_0$. The center subfigure shows the pressure contours obtained by the solving for the full network model. The right subfigure shows the pressure contours computed by the proposed method. In the computation, a 20×20 coarse blocks are used and each sampling domain is 10×10.

Table 1: The relative pressure error e_P and relative flux error e_F by using 2D-model with $N \times N$ blocks and $\delta \times \delta$ sampling domains.

	e_p			e_f		
	$\delta = 5$	$\delta = 10$	$\delta = 20$	$\delta = 5$	$\delta = 10$	$\delta = 20$
$N = 5$	0.2580	0.2522	0.2475	0.4558	0.4744	0.4758
$N = 10$	0.2912	0.2744	0.2764	0.3444	0.3575	0.3670
$N = 20$	0.0665	0.0697	0.0634	0.1022	0.0714	0.0629
$N = 40$	0.0558	0.0542	0.0546	0.0620	0.0410	0.0305

errors are less than 10% for $N = 20$ and $\delta = 5$. We only use such few information to capture the macro scale behavior correctly. The errors are large when $N = 5$, and 10 because in these cases the sampling domains do not cover the top and bottom channels. The resulted representative parameter K only capture one channel. When we increase number of coarse blocks to 20, three channels have been captured. The coarsening parameter exhibits 3 disconnected channel and the coarse scale pressure contour present the similar behavior to the network scale pressure. This numerical example shows full macroscopic model can capture the coarse scale information more accurate than 1D model.

Experiment 7. (**Homogenization to an anisotropic elliptic equation**) In this experiment, we testify the proposed macroscopic flux and iterative algorithm satisfy the results under the classical homogenization setting. Consider a network model comes from the discretization of the elliptic PDE:

$$-\nabla \cdot (a_\epsilon(\mathbf{x})\nabla u(\mathbf{x})) = 0, \quad \mathbf{x} \in [0,1] \times [0,1] \tag{35}$$

with oscillatory coefficient $a_\epsilon(\mathbf{x}) = a(\mathbf{x}/\epsilon)$, where

$$a(\mathbf{x}) = \sin(4x_1) + 0.1 \sin 2\pi(x_1 + 1.41x_2) + 0.1 \cos 2\pi x_2 + 1.20001.$$

Notice that this choice of a leads to an anisotropic homogenized equation. The anisotropic is defined by the effective diffusion tensor $\bar{A}$ whose eigenvectors do not align with vectors formed by connecting grid nodes. With this feature, we are able to test if our proposed multiscale algorithm captures the anisotropy.

We discretize the domain into 600×600 squares and each vertex represents a pore and each edge represents a throat. The conductance of the throat is the value of a at the middle point of the throat. We apply the Dirichlet boundary condition $u(\mathbf{x}) = (x_1 + 1)^2(x_2 + 1)^2$ on the boundary of the microscale network domain. The solution of the network model is a numerical approximation of the solution of (35). We discretize the network model into $N \times N$ coarse blocks and use $\delta \times \delta$ sampling domain B_δ to obtain macroscopic pressure P by our macro-micro algorithm. We use periodic boundary condition obtained from macro pressure in local network simulation.

We choose ϵ to be 0.001 and 0.0001, the sampling length δ to be 0.01, 0.0167, and N to be $6, 8, 10, 12, 15, 20, 30, 40$ and compare the value of micro-pressure p with macro-pressure P at the same position. The relative error in pressure e_p is defined as before. See Figure 10 for results.

We can observe that e_p is convergent to 0 as N increases before the error is about size ϵ, and convergence is of second order. From our error analysis in Appendix B, we know the error is control by both mocroscale and microscale discretization error and homogenization error. Macroscale discretization error is of order $1/N^2$ and homogenization error is of ϵ. When N is large enough, the error is dominated by homogenization and can not be controlled by increasing N. This coincides with the error analysis we have in Appendix B.

Because of the choice of the constant 1.41 inside the sinus function, the sampling domains does not coincide with the cell problems exactly and the estimated coefficients are different for each sampling domain. However, the error is still smaller by using $\delta = 0.01$ than using $\delta = 0.167$. This is because when $\delta = 0.01$, the sampling size is an integer multiple of ϵ for both $\epsilon = 0.001$ and $\epsilon = 0.0001$.

4 Fracturing of soft sediments

We propose a simple model to simulate propagation of a fracture in a soft (unconsolidated) sediment in this section. The purpose is to give an example of a network scale process that is not easily represented by an effective equation at the continuum scale, and to show the potential of coupling fluid and solid mechanics.

Pumping highly pressurized fluid into a sediment can cause selected throats (fluid pathways) to widen, and thereby allows the fracturing fluid to enter and extend the crack further into the formation. In our model, cracks or fractures are represented as those throats with very high conductance, while the network connectivity remains fixed. This simplified view is intuitively correct in unconsolidated sands.

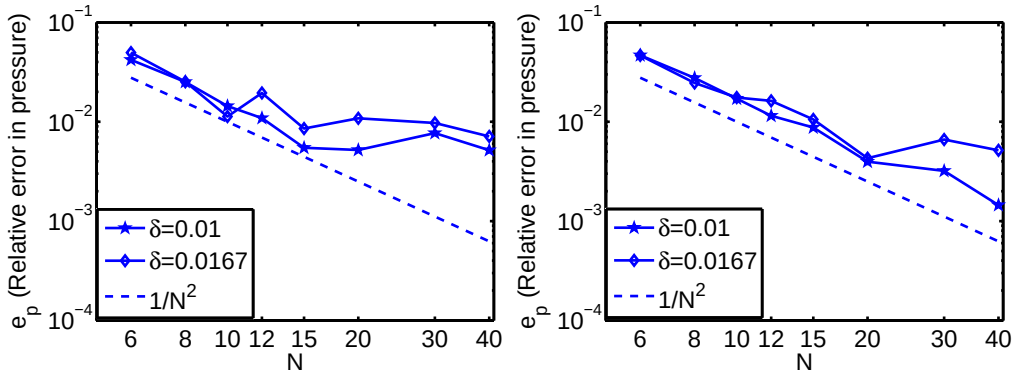

Figure 10: The relative error in pressure versus the number of coarse blocks. The left figure is the case when $\epsilon = 0.001$ and the right figure is when $\epsilon = 0.0001$. The dash line represents $y = 1/N^2$.

If a throat, such as the one depicted in Figure 11, is filled with fluid, the pore pressure acts both in normal direction to the grain walls (normal stress, shown in blue), as well as parallel to them (shear stress, shown in red).

The throat depicted will open wider if the total of normal forces (i.e. those labelled blue) pushing the grain labelled Gr_1 upwards, as well as the grain Gr_2 downwards, is larger than total of the shear forces acting on both of the grains [40, 45]. Since all forces act on the surface of the same area (length in 2D) a, when the balance is made over all of the normal (solid arrow) forces that act in y direction and divided by a, we obtain stress

$$\sigma_{\mathrm{N}} = -\frac{1}{2}(\sigma_N^{(1)} + \sigma_{\mathrm{N}}^{(2)}),$$

where

$$\sigma_{\mathrm{N}}^{(1)} \approx (p_{i,j+1} - 2p_{i,j} + p_{i,j-1}), \qquad \sigma_{\mathrm{N}}^{(2)} \approx (p_{i+1,j+1} - 2p_{i+1,j} + p_{i+1,j-1}).$$

The shear stresses (dash arrow) acting in y direction on the two grains above and below the throat are equal to $2\sigma_N$ in this case. The throat widens if the total stress is larger in magnitude than some critical value G_C, that is $G = a(\sigma_N + \sigma_T) > G_C$, where a is the length of the throat. The latter is similar to the concept of the crack extension force from plane elasticity [40, 45], and we will use the same name for it.

Note that in general, the normal and shear forces would also be balanced by gravity acting on each grain as well as the effect of earth stresses (confinement). [45] gives a simple way of incorporating earth stresses in a network setting. In our simple network, however, the grains do not touch and thus there is no way to transmit those stresses throughout the grain network. We thus impose limitations that mimic confinement effects as follows.

In our model on local network level, we modify the radii of the throats according to their extension force value. A throat is characterized as a part of fracture when its radius is close to a predefined value $r_{\max}$; this large size of radius leads to large

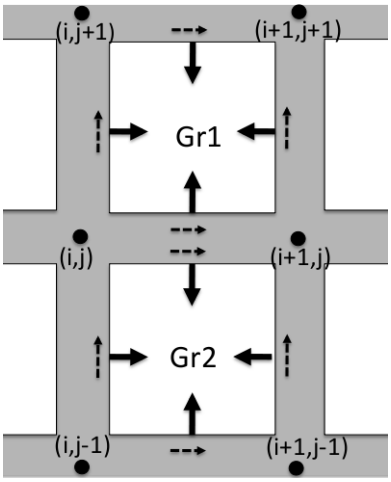

Figure 11: Illustration for computing stress using local information. Pore space (gray) and grains (white) near the throat connecting pore (i, j) and pore $(i + 1, j)$. Pore centers are marked with circles. Normal forces to grain surfaces exerted by pore pressure are depicted with solid arrows, shear forces exerted on grains by viscous forces in motion are shown by the dashed arrows.

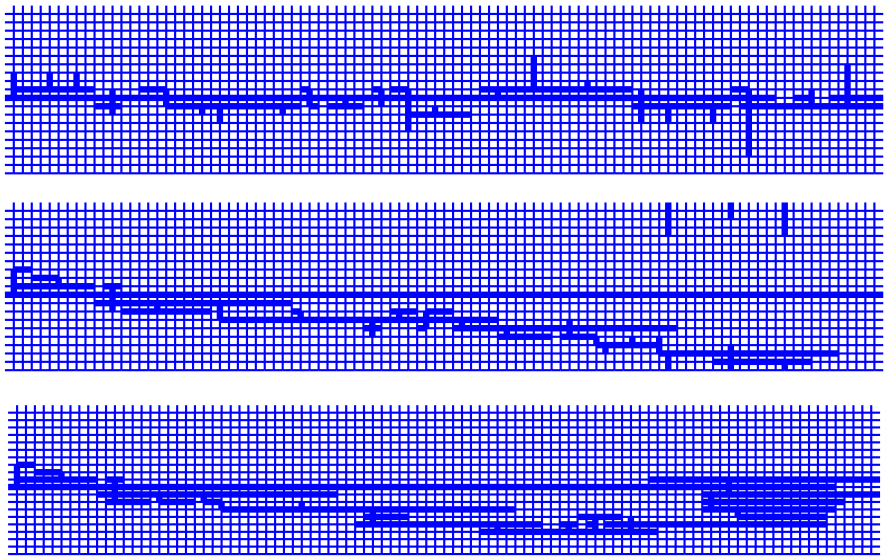

Figure 12: Snapshots of fracture simulation. The thick lines represent fracture (updated radius bigger than $8r_0$.) The top one is $c = 2$, and the middle one is $c = 2.5$ and the bottom one is $c = 4$. Note that the fracture appears to have disconnected components due to periodic boundary conditions. The fracture is connected indeed.

conductance. If a pore is connected to a throat that is identified as part of a fracture, then the pore is called a fracture node. Further, in each iteration, we check the crack extension force G of each throat that is connected to a fracture node. In case that $G > G_C$ for such a throat, we update its radius r by $r = H(G)$ for a Heaviside-like function H. Otherwise, its radius stays the same as before. Here we choose

$$H(G) = r_{\max}\frac{2}{\pi}\tan^{-1}(\frac{G - G_C}{s}) \quad \text{for} \quad G > G_C, \tag{36}$$

where $r_{\max}$ is the maximum conductance value used in the simulation and s is a suitable scaling. The conductance of this throat is then updated according to its new radius. Notice that we only update the conductance of throats connected to a fracture node and the resulting fracture is always a connected path.

We assume that once the fracture is formed, it will not close afterwards. Therefore, in our algorithm, the radius is only updated when the proposed value r_{new} is bigger than previous one r_{old}. That is

$$r_{\text{new}} = \max\{r_{\text{old}}, H(G)\}.$$

Finally, subsurface formations are under confining pressure (dependent on the depth) and cannot expand freely. In order to simulate that behavior, we confine the radii of throats by restricting the sum of the radii in each column and each row to be less than a given constant. That is, if we denote the radius of the throat connecting pore(i, j) and pore $(i+1, j)$ by $r_{i+\frac{1}{2},j}$, pore(i, j) and pore $(i, j+1)$ by $r_{i,j+\frac{1}{2}}$, then $\sum_j r_{i+\frac{1}{2},j}$ and $\sum_i r_{i,j+\frac{1}{2}}$ are bounded above by given numbers for all i and j. Therefore only certain number of throats in each row and column can be part of fracture. If the sum of the proposed radii exceed the restriction in certain column, we reassign radii to satisfy the constraint. We update throats according to the order of radii in previous step in each column and row since larger conductance is easier to expand.

Experiment 8. (**Full network simulation with the proposed fracture model**) We consider a network with pores and edges coming from a regular lattice $\mathbb{Z}^2$ over the domain $[0, 100] \times [0, 20]$. We set $p = 1$ at the left boundary and $p = 0$ on the right, and periodic in the two horizontal boundaries. The initial radii of throats are randomly generated from the uniform distribution $[(1-\lambda)r_0, (1+\lambda)r_0]$ with $r_0 = 0.01$ and $\lambda = 0.5$, except for the conductance of the throat connecting pore $(1, 11)$ to pore $(2, 11)$. The conductance for that particular throat is set to be $r_{\max} = 10r_0 = 0.1$ as the initial onset of a fracture in the network. We use the linear flux-pressure gradient relation as in Experiment 2 to compute pressure in each fixed state. Then we update conductance according to the computed pressure. The critical crack extension force G_C for each throat is a constant with a small random perturbation. The random perturbation reflects the fact that some locations are easier fractured than others in reality. The upper bound of the sum of radii is $20cr_0$ in each columns and $100cr_0$ in each row. We choose c to be $2, 2.5$ and 4. When a updated radius becomes bigger than $8r_0$, the throat is marked as a part of fracture. See Figure 12 for snap shots of simulations involving different c. We can see the fracture is more concentrated when c

is small and spread out when c is large. However, the fracture pattern stay unchanged when c is larger than 4. This is the effect resulting from the constraint on the sum of throat radii. Finally, we notice that even though the network model used in the simulations are constructed from a regular grid, sufficiently irregular fractures could still develop.

Experiment 9. (**Multiscale simulations with the fracture model in local networks**) In this experiment, we incorporate our quasi-static fracture development model for two dimensional networks into the multiscale algorithm. We consider a full network consisting of pores and edges taken from a regular Cartesian lattice over the domain $[0, 10000] \times [0, 20]$. No source inside the network and the boundary conditions are Dirichlet in x-direction with $p = 1000$ and $p = 0$ on left and right hand side and periodic in the two horizontal boundaries. The radii of throats are initially randomly generated from the uniform distribution $[(1 - \lambda)r_0, (1 + \lambda)r_0]$ with $r_0 = 0.01$ and $\lambda = 0.5$, we choose the viscosity $\mu = 1$. We divide the whole network into 10 blocks, and evaluate the macroscopic fluxes by simulations using local networks obtained from the 101×20 pores centering at each block and use the linear flux-pressure gradient relation as in Experiment 2 to compute pressure in each local network.

We now apply our quasi-static fracture development model described as in Experiment 8 on the first local network, and the rest local networks stay unchanged. The conductance connecting pore $(1, 11)$ to pore $(2, 11)$ in the first local network is set to be $r_{max} = 10r_0 = 0.1$ to represent initialization of a fracture. Then we develop fracture in the first block until it stops or reaches the right hand side of the block. In addition to the rules to develop fracture in Experiment 8, we impose an additional condition to control fracture development. In each static state, there is a $1 - \gamma$ probability that we stop fracture development. We compute P_i in each fix static state and set $\gamma = 0.994^{1/(P_0 - P_1)}$. It means the larger macro pressure gradient the higher chance to propagate the fracture. The number 0.994 is chosen by $0.55^{1/100}$ and therefore it has roughly 0.55 probability for fracture to reach the right hand side of the first block.

If fracture reaches the right hand side of the first block, then we keep developing fracture in the second block. We initialize a fracture in the second block by setting the radii of the throats connected to the fracture nodes in the second local network to be $10r_0$ and perform the same fracture development simulation. Now the probability $\gamma = 0.994^{1/(P_1 - P_2)}$ and the rest local networks stay unchanged. Inductively, we continue this process until the fracture development stops or reaches the right hand side of the last local network domain to obtain final macro pressure P and flux F.

We run 1000 realizations on initial conductances and compare the macro pressure and the flux obtained from fracture development simulation with thew macro pressure and flux obtained from the original conductances. Figure 13 shows that the pressure profiles change rather non-trivially according different fracture configurations that developed in the simulations (the left figure), and in contrast pressure profiles are essentially linear without the fracture model (the right figure). Since conductance is uniformly distributed we can expect the effective permeability is almost the same for each constant if no fracture development is involved. Therefore the macro pressure is

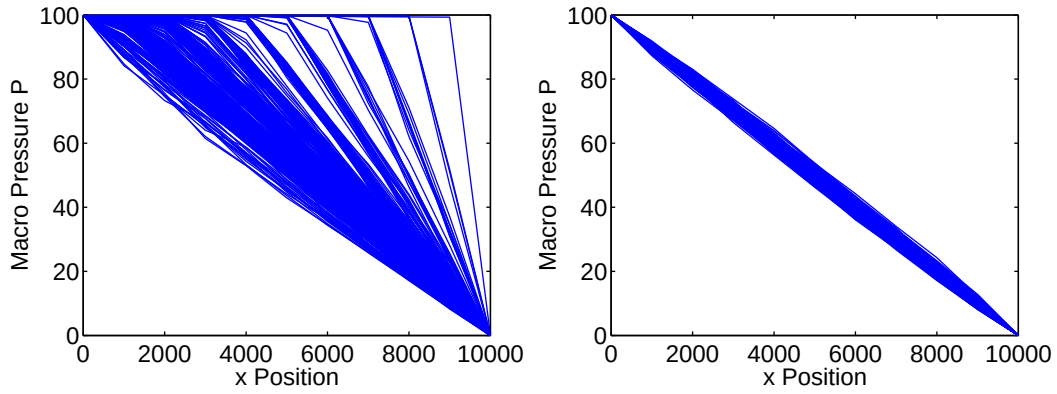

Figure 13: Comparison of macro scale pressure profile. The left hand side figure is the pressure profile of 1000 realizations with fracture development. The right hand side figure is the pressure profile of 1000 realizations without any modification on radii of throat.

almost linear. On the other hand, when fracture development reaches an equilibrium, the effective permeability of the local network becomes larger than those without fracture development. Hence the flux with fracture development is larger than the flux without fracture development; this is a natural consequence since fractures increase effective permeability. Figure 15 shows the histograms of the fluxes computed from our simulations using different random realizations of the underlying networks conductances. We can see the fluxes without fracture development form a bell shape distribution with very small deviation. On the other hand, the fluxes from simulations with fracture development form a significantly different distribution. Here,we report the total fluxes through the entire network. If we use $r_0 = 0.01$ to compute the effective conductance, we get $K \simeq \pi r_0^4/(8\mu) \cdot 20$ and therefore, the flux is $K\nabla P \simeq 7.854 \cdot 10^{-9}$.

5 Acknowledgements

Chu, Engquist, and Tsai are partially supported by NSF DMS-0714612, and NSF DMS-0914840.

A Properties of Network models

We present two simple properties of network models in this section.

Lemma A.1. *Suppose that any two nodes in the domain are connected by a continuous path of throats, and the conductance $c_{ij} > 0$ for each i and $j \in I_i$. Then the pressure p satisfies the maximal and minimal principle, i.e.,*

$$\max_{i\in I}\{p_i\} = \max_{i\in I\setminus I^{(0)}}\{p_i\}, \quad \textit{and} \quad \min_{i\in I}\{p_i\} = \min_{i\in \setminus I^{(0)}}\{p_i\}.$$

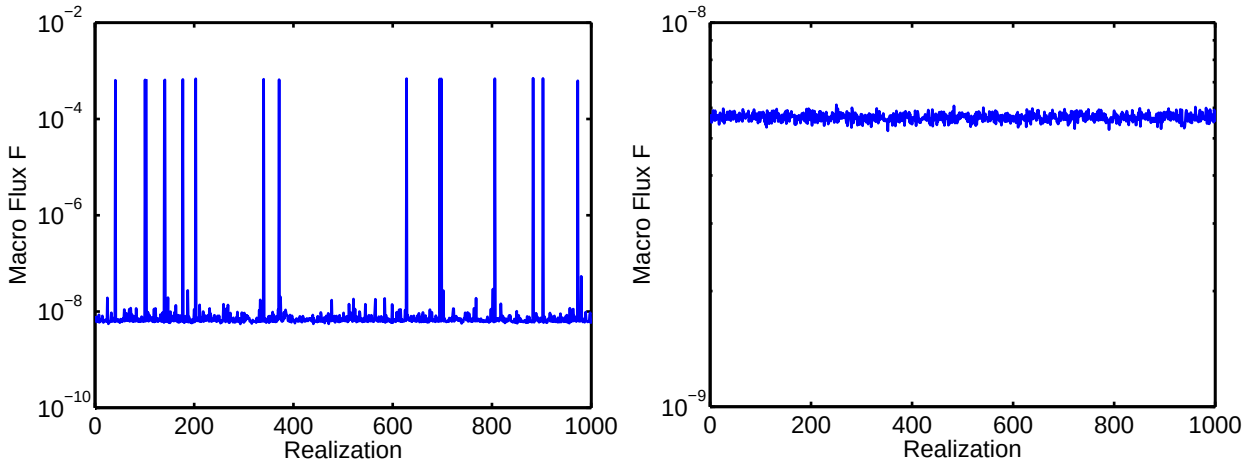

Figure 14: Comparison of macro scale flux in each realization. The left figure is the flux with fracture development and the right figure is the flux without fracture development.

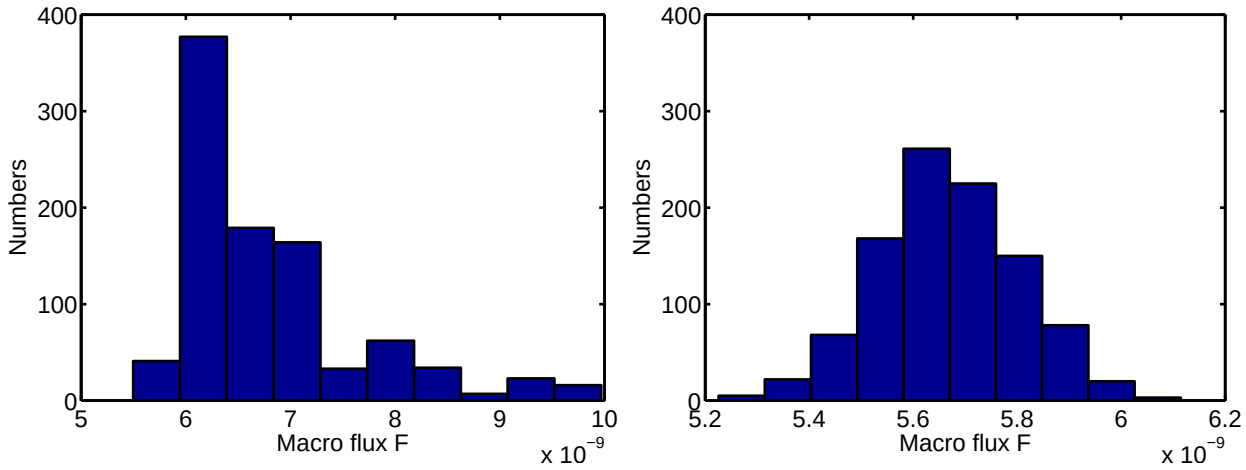

Figure 15: Histogram of flux. The left figure is the flux with fracture development and the right figure is the flux without fracture development. We omit those realizations that resulted in very large fluxes in the left figure.

Proof. By contradiction, suppose that maximum is attained at an interior node; i.e. $\max_{i\in I^{(0)}}\{p_i\} > \max_{i\in I\setminus I^0}\{p_i\}$. Let I_M denote the largest index set containing all index i such that $p_i = \max_{j\in I}\{p_j\}$. Then $I_M \subseteq I^{(0)} \subset I$ and there exist indices $i_* \in I_M$ and $j_* \in I_{i_*}$ such that $j_* \notin I_M$. Since $p_{i_*} = \max_{i\in I}\{p_i\}$ and $c_{ij} > 0$, we have

$$\sum_{j\in I_{i_*}} c_{i_*,j}(p_{i_*} - p_j) \geq c_{i_*,j_*}(p_{i_*} - p_{j_*}) > 0$$

which contradicts to (4). The proof of the minimal principle is analogous. □

Lemma A.2. *Suppose any two nodes in the network can be connected by a continuous path of throats, and the conductance $c_{ij} > 0$ and is independent of p_i and p_j for all $i \in I$, $j \in I_i$.*

1. *Then there exists a unique solution $\{p_i\}_{i\in I^{(0)}}$ satisfying (4) and the Dirichlet boundary conditions at the left and the right network boundaries, and periodic condition in the remaining faces.*
2. *If the conductance c_{ij} is also independent of P_R and P_L, then there exists a nonnegative constant k depending only on c_{ij} such that the flux take the form*

$$f = -k(P_R - P_L)/\delta,$$

where δ is the distance between left face and right face.

Proof. Rewritten (4) as

$$C\mathbf{p} = \mathbf{b}, \tag{37}$$

where $\mathbf{p}$ is the vector whose entries are p_i for $i \in I^{(0)}$ and $\mathbf{b}$ is determined by the boundary conditions P_R and P_L. Since C is a square matrix independent of $\mathbf{p}$, it suffices to show that C is injective. Suppose $\mathbf{b} = \mathbf{0}$, then it is easy to see $P_L = P_R = 0$. Max-Min principle (Lemma A.1) implies $\mathbf{p} = \mathbf{0}$. Hence C is invertible and $\mathbf{p}$ is uniquely solvable.

Let $\mathbf{p}_*$ be the solution of (37) with $P_R = 1$ and $P_L = 0$ and $\mathbf{p}$ be the solution of (37) with arbitrary P_R and P_L. By linearity of the system (37), $\mathbf{p} = (P_R - P_L)\mathbf{p}_* + P_L$. Denoting the flux resulting from the boundary values P_R, P_L by $f(P_L, P_R)$, we see that $f(P_L, P_R) = (P_R - P_L)f(1, 0)$. Let $k = -f(1, 0)\delta$. It is clear that $k > 0$ as a consequence of the maximal-minimal principle, and $f(P_L, P_R) = -k(P_R - P_L)/\delta$. □

B Error Analysis for the Elliptic Homogenization Case

In this section, we investigate the error between the microscopic pressure and macroscopic pressure computed by our method. Our observation is that equation (3) can be interpreted as a discretization of an elliptic problem under some assumption on the network configuration. For such systems, we can estimate the accuracy of our proposed multiscale method via (numerical) homogenization theory.

For simplification, we only demonstrate two dimensional case, but the argument works for higher dimensional cases also. Let $\Omega = [x_L, x_R] \times [y_B, y_T]$ be a rectangular domain. Consider the following elliptic equation

$$-\nabla \cdot (a_\epsilon(\mathbf{x})\nabla p_\epsilon(\mathbf{x})) = 0, \quad \mathbf{x} \in \Omega; \quad p_\epsilon(\mathbf{x}) = g(\mathbf{x}), \quad \mathbf{x} \in \partial\Omega; \tag{38}$$

where $a_\epsilon(\mathbf{x}) := a(\mathbf{x}, \mathbf{x}/\epsilon)$ for some positive smooth function $a(\mathbf{x}, \mathbf{y})$ that is periodic in $\mathbf{y}$ with period 1 in first and second coordinates for any fixed $\mathbf{x}$, and g is the given Dirichlet boundary condition. The parameter ϵ is a small positive number that refers to the length scale of rapid oscillation of coefficient. We divide the domain into $n \times m$ partitions and let $\delta x = (x_R - x_L)/n$, $x_i = x_L + i\delta x$ and $\delta y = (y_T - y_B)/m$, $y_j = y_B + j\delta x$, where n and m are chosen large enough to resolve ϵ scale. Let $\mathbf{x}_{i,j} = (x_i, y_j)$. We discretize(38) by

$$\begin{aligned} -a_\epsilon(\mathbf{x}_{i+\frac{1}{2},j})\frac{p_{i+1,j} - p_{i,j}}{\delta x} + a_\epsilon(\mathbf{x}_{i-\frac{1}{2},j})\frac{p_{i,j} - p_{i-1,j}}{\delta y} \\ - a_\epsilon(\mathbf{x}_{i,j+\frac{1}{2}})\frac{p_{i,j+1} - p_{i,j}}{\delta x} + a_\epsilon(\mathbf{x}_{i,j-\frac{1}{2}})\frac{p_{i,j} - p_{i,j-1}}{\delta y} = 0 \end{aligned} \tag{39}$$

where $\mathbf{x}_{i+\frac{1}{2},j}$ is the middle point (quadrature point) of $\mathbf{x}_{i.j}, \mathbf{x}_{i+1,j}$ and $p_{i,j}$ is the nodal value of the finite element solution to approximate $p_\epsilon(\mathbf{x}_{i,j})$. By standard convergence theory, we have

$$\|p_{i,j} - p_\epsilon(\mathbf{x}_{i,j})\| < C_1(\epsilon, a)h^2, \tag{40}$$

where $h = \max\{\delta x, \delta y\}$ and $C_1(\epsilon, a)$ is a constant independent of h but may depend on a, ϵ and boundary value g.

On the other hand, the discrete system defined in (39) can be viewed as equations of conservation law of a linear network model for pressures $p_{i,j}$ pores; see equation (4): the graph of the network model is simply square lattice grids and each pore connects to four adjacent pores. The conductance $c_{i+\frac{1}{2},j}$ of the throat connecting pore (i, j) and pore $(i+1, j)$ is given by

$$c_{i+\frac{1}{2},j} = a_\epsilon(\mathbf{x}_{i+\frac{1}{2},j})/\delta x,$$

and conductance $c_{i,j+\frac{1}{2}}$ of the throat connecting pore (i, j) and pore $(i, j+1)$ is defined analogously.

Suppose we apply the macroscopic 2D model and macro-micro algorithm to this network model. Then the macroscopic pressure $\mathbf{P}$ satisfies

$$\begin{aligned} -K^{1,1}_{k+\frac{1}{2},l}D^x_+P_{k,l} + K^{1,1}_{k-\frac{1}{2},l}D^x_-P_{k,l} - K^{2,2}_{k,l+\frac{1}{2}}D^y_+P_{k,l} \\ + K^{2,2}_{k,l-\frac{1}{2}}D^y_-P_{k,l} - K^{1,2}_{k+\frac{1}{2},l}D^y_0P_{k+\frac{1}{2},l} + K^{1,2}_{k-\frac{1}{2},l}D^y_0P_{k-\frac{1}{2},l} \\ - K^{2,1}_{k,l+\frac{1}{2}}D^x_0P_{k,l+\frac{1}{2}} + K^{2,1}_{k,l-\frac{1}{2}}D^x_0P_{k,l-\frac{1}{2}} = 0 \end{aligned} \tag{41}$$

where $K_{k\pm\frac{1}{2},l}$'s and $K_{k,l\pm\frac{1}{2}}$'s are obtained from local network simulation discussed in section 3 with local network on B_δ. Here we omit the upper index (n) since the network is linear, $K_{k\pm\frac{1}{2},l}$'s and $K_{k,l\pm\frac{1}{2}}$'s are constants independent of macroscopic pressure $\mathbf{P}$.

Our goal is to study the error between the macroscopic pressure $\mathbf{P}$ and the microscopic pressure p_ϵ by using techniques in homogenization.

The homogenized equation of (38) is simply

$$-\nabla \cdot \left(\bar{A}(x)\nabla \overline{P}\right) = 0, \quad \mathbf{x} \in \Omega; \quad \overline{P}(\mathbf{x}) = g(\mathbf{x}), \quad \mathbf{x} \in \partial\Omega \tag{42}$$

where $\bar{A}$ is the homogenized coefficient which can be obtained by solving a cell problem (See [12] for more detail). Then standard homogenization theory has that

$$\|\overline{P} - p_\epsilon\|_\infty < C_2(a)\epsilon, \tag{43}$$

where the constant C_2 depends on a only.

Notice that $\bar{A}$ can be a nondiagonal 2×2 matrix even a is a scalar. We use $\bar{A}^{i,j}$ to denote which the (i,j) entry of $\bar{A}$. The homogenized equation can be discretized by

$$\begin{aligned} -\bar{A}^{1,1}(\mathbf{y}_{k+\frac{1}{2},l})D_+^x\overline{P}_{k,l} + \bar{A}^{1,1}(\mathbf{y}_{k-\frac{1}{2},l})D_-^x\overline{P}_{k,l} - \bar{A}^{2,2}(\mathbf{y}_{k,l+\frac{1}{2}})D_+^y\overline{P}_{k,l} \\ + \bar{A}^{2,2}(\mathbf{y}_{k,l-\frac{1}{2}})D_-^y\overline{P}_{k,l} - \bar{A}^{1,2}(\mathbf{y}_{k+\frac{1}{2},l})D_0^y\overline{P}_{k+\frac{1}{2},l} + \bar{A}^{1,2}(\mathbf{y}_{k-\frac{1}{2},l})D_0^y\overline{P}_{k-\frac{1}{2},l} \\ - \bar{A}^{2,1}(\mathbf{y}_{k,l+\frac{1}{2}})D_0^x\overline{P}_{k,l+\frac{1}{2}} + \bar{A}^{2,1}(\mathbf{y}_{k,l-\frac{1}{2}})D_0^x\overline{P}_{k,l-\frac{1}{2}} = 0 \end{aligned} \tag{44}$$

where $\mathbf{y}_{k,l} = (x_L + k\Delta x, y_B + l\Delta y)$ and $\mathbf{y}_{l+\frac{1}{2}}$ is the middle point (quadrature point) of $\mathbf{y}_{k,l}$ and $\mathbf{y}_{k+1,l}$. Again, we have the estimate

$$\|\overline{P}_{k,l} - \overline{P}(\mathbf{y}_{k,l})\| < C_3(a)H^2, \tag{45}$$

where $H = \max\{\Delta x, \Delta y\}$ and C_3 is independent of H. We observe that $\overline{P}_{k,l}$ and $P_{k,l}$ satisfy similar equations (41) and (44). If we can estimate the difference between coefficients in (41) and (44), then we have error estimate between $\overline{P}_{k,l}$ and $P_{k,l}$.

Let V be a piecewise linear function on $B_\delta(\mathbf{y}_{k+\frac{1}{2},l})$ that is a square centered at the quadrature point $\mathbf{y}_{k+\frac{1}{2},l}$ with length δ. For each linear function V and $B_\delta(\mathbf{y}_{k+\frac{1}{2},l})$, let v_ϵ be the solution of

$$\begin{aligned} -\nabla \cdot (a_\epsilon(\mathbf{x})\nabla v_\epsilon(\mathbf{x})) = 0, \quad \mathbf{x} \in B_\delta(\mathbf{y}_{l+\frac{1}{2}}) \\ v_\epsilon(\mathbf{x}) = V(\mathbf{x}), \quad \mathbf{x} \in \partial B_\delta(\mathbf{y}_{l+\frac{1}{2}}) \end{aligned} \tag{46}$$

The HMM method [23] suggests to estimate the homogenized coefficient $\overline{A}$ at quadrature point by A_H, which is defined as

$$\nabla W A_H(\mathbf{y}_{k+\frac{1}{2},l})\nabla V = \frac{1}{\delta^2}\int_{B_\delta(\mathbf{y}_{k+\frac{1}{2},l})} \nabla w_\epsilon(\mathbf{x})a_\epsilon(\mathbf{x})\nabla v_\epsilon(\mathbf{x})\, d\mathbf{x},$$

where v_ϵ and w_ϵ are solutions of (46) associated with V and W respectively. Notice that (46) implies

$$\int_{B_\delta(\mathbf{y}_{k+\frac{1}{2},l})} \nabla(w_\epsilon(\mathbf{x}) - W)a_\epsilon(\mathbf{x})\nabla v_\epsilon(\mathbf{x})\, d\mathbf{x} = 0$$

Therefore we have

$$\nabla W A_H(\mathbf{y}_{k+\frac{1}{2},l})\nabla V = \nabla W \cdot \left(\frac{1}{\delta^2} \int_{B_\delta(\mathbf{y}_{k+\frac{1}{2},l})} a_\epsilon(\mathbf{x})\nabla v_\epsilon(\mathbf{x})\, d\mathbf{x} \right) = \nabla W \cdot F(\nabla V),$$

where $F(\nabla V)$ is the average of $a_\epsilon(\mathbf{x})\nabla v_\epsilon(\mathbf{x})$ on B_δ.

On the other hand, the local network solution $p_{i,j}$ for computing local flux $\hat{f}$ in our scheme is exactly the discrete solution of (46) using grid size δx and δy with boundary condition given by linear interpolation of a linear function obtained from $P_{k,l}$, $P_{k+1,l}$, $P_{k,l+1}$, $P_{k+1,l+1}$, $P_{k,l-1}$, $P_{k+1,l-1}$. And our local flux $\hat{f}$ is mean value of discrete flux in each throats. Since the discretization has second order accuracy in pressure, we have first order accuracy in flux and also its mean value:

$$\|F(\nabla P) - \hat{f}\| \le C_1 h.$$

By choosing ∇W to be $[1,0]^T$ and $[0,1]^T$ and using the definition of K's in our algorithm with the above flux estimate, we get

$$|A_H^{1,m}(\mathbf{y}_{k\pm\frac{1}{2},l}) - K^{1,m}_{k\pm\frac{1}{2},l}| \le C_1 h, \quad |A_H^{2,m}(\mathbf{y}_{k,l\pm\frac{1}{2}}) - K^{2,m}_{k,l\pm\frac{1}{2}}| \le C_1 h$$

for $m = 1, 2$. By triangle inequality, we obtain the error between coefficients:

$$\begin{aligned} |K_{k+\frac{1}{2},l} - \bar{A}(\mathbf{y}_{k+\frac{1}{2},l})| &\le |K^{1,m}_{l+\frac{1}{2}} - A_H^{1,m}(y_{l+\frac{1}{2}})| + |A_H^{1,m}(y_{l+\frac{1}{2}}) - \bar{A}^{1,m}(y_{l+\frac{1}{2}})| \\ &\le C_1 h + e(\text{HMM}), \end{aligned} \tag{47}$$

where $e(\text{HMM}) = \|A_H(\mathbf{y}_{k+\frac{1}{2},l}) - \bar{A}(\mathbf{y}_{k+\frac{1}{2},l})\|$. Combining (41), (44) and (47), it leads to

$$\|\overline{P}_{k,l} - P_{k,l}\| \le C_5(e(\text{HMM}) + h) \tag{48}$$

Denote i_k, j_l the indices such that $\mathbf{x}_{i_k,j_l} = \mathbf{y}_{k,l}$, for each k and l. Using (40), (45), (43) and (48), we obtain the final estimate

$$\begin{aligned} \|P_{k,l} - p_{i_k,j_l}\| &\le \|P_{k,l} - \overline{P}_{k,l}\| + \|\overline{P}_{k,l} - \overline{P}(\mathbf{y}_{k,l})\| + \|\overline{P}(\mathbf{y}_{k,l}) - p_\epsilon(\mathbf{y}_{k,l})\| + \|p_\epsilon(\mathbf{y}_{k,l}) - p_{i_k,j_l}\| \\ &< C_1(\epsilon, a)h + C_6(a)(H^2 + \epsilon + e(\text{HMM})). \end{aligned} \tag{49}$$

Recall that the HMM error $e(\text{HMM})$ can be controlled by

$$e(\text{HMM}) \le \begin{cases} C_4\epsilon, & \text{if } \delta = \epsilon \\ C_4(\delta + \epsilon/\delta), & \text{else} \end{cases} \tag{50}$$

See [26] for more reference. Summarizing above discussion, we have proved

Theorem B.1. *Given a 2D linear network model whose graph is simply a lattice grids, and each pores connect to adjacent four pores. Suppose the conductance $c_{i+\frac{1}{2},j}$ of the throat connecting pore (i,j) and pore $(i+1,j)$ is given by*

$$c_{i+\frac{1}{2},j} = a_\epsilon(\mathbf{x}_{i+\frac{1}{2},j})/\delta x,$$

and the conductance $c_{i,j+\frac{1}{2}}$ *of the throat connecting pore* (i,j) *and pore* $(i,j+1)$ *is given by*

$$c_{i,j+\frac{1}{2}} = a_\epsilon(\mathbf{x}_{i,j+\frac{1}{2}})/\delta x,$$

where $a_\epsilon(x) = a(x, x/\epsilon)$ *for some continuous* $a(\mathbf{x}, \mathbf{y})$ *and* a *is periodic function in* $\mathbf{y}$ *with period 1. Let* $p_{i,j}$ *be the pressure of the network model and* $P_{k,l}$ *is the macroscopic pressure computed from macro-micro algorithm with sampling size* δ*. Let* i_k, j_l *denote the index such that* p_{i_k,j_l} *and* $P_{k,l}$ *are at the same point. Then there exists constants* C *and* D *such that*

$$\|P_{k,l} - p_{i_k,j_l}\| < \begin{cases} C(\epsilon,a)h + D(a)(H^2+\epsilon), & \text{if } \delta = \epsilon \\ C(\epsilon,a)h + D(a)(H^2+\epsilon+\delta+\frac{\epsilon}{\delta}), & \text{else} \end{cases} \tag{51}$$

where C *depends on* a *and* ϵ*, and* D *depends on* a *only.*

References

[1] J. E. Aarnes, Y. Efendiev, and L. Jiang. Mixed multiscale finite element methods using limited global information. *Multiscale Model. Simul.*, 7(2):655–676, 2008.

[2] A. Abdulle and W. E. Finite difference heterogeneous multi-scale method for homogenization problems. *J. Comput. Phys.*, 191(1):18–39, 2003.

[3] T. Arbogast. Gravitational forces in dual-porosity systems: 1. model derivation by homogenization. *Transport in Porous Media*, 13(2):179–203, 1993.

[4] T. Arbogast. Gravitational forces in dual-porosity systems: 2. computational validation of the homogenized model. *Transport in Porous Media*, 13(2):205–220, 1993.

[5] T. Arbogast, L.C. Cowsar, M.F. Wheeler, and I. Yotov. Mixed finite element methods on nonmatching multiblock grids. *SIAM J. Numer. Anal.*, 37(4):1295–1315, APR 27 2000.

[6] G. Ariel, B. Engquist, and R. Tsai. A multiscale method for highly oscillatory ordinary differential equations with resonance. *Math. Comp.*, 78(266):929–956, 2009.

[7] I. Babuška, G. Caloz, and J. E. Osborn. Special finite element methods for a class of second order elliptic problems with rough coefficients. *SIAM J. Numer. Anal.*, 31(4):945–981, 1994.

[8] I. Babuška and J. E. Osborn. Generalized finite element methods: their performance and their relation to mixed methods. *SIAM J. Numer. Anal.*, 20(3):510–536, 1983.

[9] M. T. Balhoff, K. E. Thompson, and M Hjortso. Coupling pore-scale networks to continuum-scale models of porous media. *Computers and Geosciences*, 33(3):393–410, 2007.

[10] Matthew Balhoff, Sunil Thomas, and Mary Wheeler. Mortar coupling and upscaling of pore-scale models. *Computational Geosciences*, 12:15–27, 2008. 10.1007/s10596-007-9058-6.

[11] Javad Behseresht, Steven L. Bryant, and Kamy Sepehrnoori. Infinite-Acting Physically Representative Networks for Capillarity-Controlled Displacements. *SPE JOURNAL*, 14(4):568–578, DEC 2009.

[12] A. Bensoussan, J. L. Lions, and G. Papanicolaou. *Asymptotic analysis for periodic structures*, volume 5 of *Studies in Mathematics and its Applications*. North-Holland Publishing Co., Amsterdam, 1978.

[13] Stewart W. E. Bird, R. B. and E. N. Lightfoot. *Transport Phenomena*. John Wiley and Sons, New York, 2007.

[14] M.J. Blunt. Flow in porous media - pore-network models and multiphase flow. *Current Opinion Colloid Interface Sci.*, 6:197–207, 2001.

[15] M.J. Blunt, M.D. Jackson, M. Piri, and P.H. Valvatne. Detailed physics, predictive capabilities and macroscopic consequences for pore-network models of multiphase flow. *Adv. Water. Resour.*, 25:1069–1089, 2002.

[16] C. G. Broyden. A class of methods for solving nonlinear simultaneous equations. *Math. Comp.*, 19:577–593, 1965.

[17] S.L. Bryant, P.R. King, and D.W. Mellor. Network model evaluation of permeability and spatial correlation in a real random sphere packing. *Transport Porous Media*, 11:53–70, 1993.

[18] M.A. Celia, P.C. Reeves, and L.A. Ferrand. Recent advances in pore-scale models for multiphase flow in porous media. *Rev. Geophys. Suppl.*, 33:1049–1057, 1995.

[19] J. Chu, Y. Efendiev, V. Ginting, and T. Y. Hou. Flow based oversampling technique for multiscale finite element methods. *Adv. Wat. Res.*, 31:599–608, 2008.

[20] A.B. Dixit, J.S. Buckley, S.R. McDougall, and K.S. Sorbie. Empirical measures of wettability in porous media and the relationship between them derived from pore-scale modelling. *Transport Porous Media*, 40:27–54, 2000.

[21] L. J. Durlofsky, Y. Efendiev, and V. Ginting. An adaptive local-global multiscale finite volume element method for two-phase flow simulations. *Adv. Wat. Res.*, 30:576–588, 2007.

[22] W. E. Analysis of the heterogeneous multiscale method for ordinary differential equations. *Commun. Math. Sci.*, 1(3):423–436, 2003.

[23] W. E and B. Engquist. The heterogeneous multi-scale methods. *Comm. Math. Sci*, 1(1):87–133, 2003.

[24] W. E, B. Engquist, X. Li, W. Ren, and E. Vanden-Eijnden. Heterogeneous multiscale methods: a review. *Commun. Comput. Phys.*, 2(3):367–450, 2007.

[25] W. E, D. Liu, and E. Vanden-Eijnden. Analysis of multiscale methods for stochastic differential equations. *Comm. Pure Appl. Math.*, 58(11):1544–1585, 2005.

[26] W. E, P. B. Ming, and P. W. Zhang. Analysis of the heterogeneous multiscale method for elliptic homogenization problems. *J. Amer. Math. Soc.*, 18(1):121–156 (electronic), 2005.

[27] Y. Efendiev, V. Ginting, and T. Y. Hou. Multiscale finite element methods for nonlinear partial differential equations. *Comm. Math. Sci.*, 2(4):553–589, 2004.

[28] Y. Efendiev, V. Ginting, T. Y. Hou, and R. Ewing. Accurate multiscale finite element methods for two-phase flow simulations. *J. Comput. Phys.*, 220(1):155–174, 2006.

[29] Y. Efendiev and T. Y. Hou. *Multiscale finite element methods: Theory and applications*. Springer, New York, 2009.

[30] B. Engquist, H. Holst, and O. Runborg. Multi-scale methods for wave propagation in heterogeneous media. *Commun. Math. Sci*, Accepted, 2010.

[31] B. Engquist and Y.-H. Tsai. Heterogeneous multiscale methods for stiff ordinary differential equations. *Math. Comp.*, 74(252):1707–1742, 2005.

[32] I. Fatt. The network model of porous media I. Capillary characreristics. *Pet. Trans. AIME*, 207:144–159, 1956a.

[33] I. Fatt. The network model of porous media II. Dynamic properties of a single size tube network. *Pet. Trans. AIME*, 207:160–163, 1956b.

[34] I. Fatt. The network model of porous media III. Dynamic properties of networks with tube radius distribution. *Pet. Trans. AIME*, 207:164–181, 1956c.

[35] P. Forchheimer. *Hydrolik*. Teubner, Leipzig and Berlin, 1914.

[36] M. Hilpert and C.T. Miller. Pore-morphology-based simulation of drainage in totally wetting porous media. *Adv. Water. Resour.*, 24:243–255, 2001.

[37] T. Y. Hou and X.-H. Wu. A multiscale finite element method for elliptic problems in composite materials and porous media. *J. Comput. Phys.*, 134(1):169–189, 1997.

[38] T. Y. Hou, X.-H. Wu, and Z. Cai. Convergence of a multiscale finite element method for elliptic problems with rapidly oscillating coefficients. *Math. Comp.*, 68(227):913–943, 1999.

[39] M. Karimi-Fard, B. Gong, and L. J. Durlofsky. Generation of coarse-scale continuum flow models from detailed fracture characterization. *Water Res. Research*, 42(10), 2007.

[40] B. Lawn. *Fracture of Brittle Solids*. Cambridge University Press, Cambridge, 1993.

[41] X. Li and W. E. Multiscale modeling of the dynamics of solids at finite temperature. *J. Mech. Phys. Solids*, 53(7):1650–1685, 2005.

[42] P.E. Oren and S. Bakke. Reconstruction of Berea sandstone and pore-scale modelling of wettability effects. *J. Petroleum Sci. Eng.*, 39:177–199, 2003.

[43] P.C. Reeves and M.A. Celia. A functional relationship between capillary pressure, saturation, and interfacial area as revealed by a pore scale network model. *Water Resour. Res.*, 32:2345–2358, 1996.

[44] W. Ren and W. E. Heterogeneous multiscale method for the modeling of complex fluids and micro-fluidics. *J. Comput. Phys.*, 204(1):1–26, 2005.

[45] T. Reuschle. A network approach to fracture: The effect of heterogeneity and loading conditions. *Pure Appl. Geophys.*, 152:641–665, 1998.

[46] F. D. Rossa, C. D'Angelo, and A. Quarteroni. A distributed model of traffic flows on extended regions. *Networks and Heterogeneous Media*, 5(3), 2010.

[47] F. Thauvin and K. K. Mohanty. Network modeling of non-darcy flow through porous media. *Transport in Porous Media*, 31:19–37, 1998.

[48] P.H. Valvatne and M.J. Blunt. Predictive pore-scale modeling of two-phase flow in mixed wet media. *Water Resour. Res.*, 40:W07406, 2004.

[49] M.I.J. van Dijke, K.S. Sorbie, and S.R. McDougall. Saturation-dependencies of three-phase relative permeabilities in mixed-wet and fractionally wet systems. *Adv. Water. Resour.*, 24:365–384, 2001.

[50] E. Vanden-Eijnden. Numerical techniques for multi-scale dynamical systems with stochastic effects. *Commun. Math. Sci.*, 1(2):385–391, 2003.

[51] X. Wang and K.K. Mohanty. Pore-network model of flow in gas-condensate reservoirs. *SPE J.*, 5:426–34, 2000.

[52] J. Young and S. Mitran. A continuum-microscopic algorithm for modeling fibrous, heterogeneous media with dynamic microstructures. *Multiscale Model. Simul.* To appear.

[53] S. Youssef, M. Han, D. Bauer, E. Rosenberg, S. Bekri, M. Fleury, and O. Vizika. High resolution μCT combined to numerical models to assess electrical properties of bimodal carbonates. Abu Dhabi, UAE, 29 October - 2 November 2008.